Microscopy Driven Characterization of Human Brown Adipose Spheroids.

By Aima Sajjad

UNIVERSITY OF TURKU

Master's Thesis

University of Turku

Department of Medicine

25.04.2026

Master's degree in Biomedical Imaging
Specialization theme

Credits: 40

Supervisors:

1. Kirsi A. Virtanen - Turku PET Centre (University of Turku and Turku University Hospital)
2. Francisco Miguel Acosta Manzano - Turku PET Centre (University of Turku and Turku University Hospital)
3. Johanna Örling - Turku PET Centre (University of Turku and Turku University Hospital)

The originality of this thesis has been checked in accordance with the University of Turku quality assurance system using the Turnitin Originality Check service.

Abstract

UNIVERSITY OF TURKU
Faculty of Medicine
Institute of Biomedicine

Author: Aima Sajjad
Title: Microscopy Driven Characterization of Human Brown Adipose Spheroids.

Supervisors: Kirsi A. Virtanen, Francisco M. Acosta Manzano and Johanna Örling.
Master's Thesis, 53 pp., 1 Appendices
Biomedical Imaging
April 2026

Brown adipose tissue (BAT) is an adipose tissue (AT) that dissipates chemical energy as heat through uncoupling protein 1 (UCP1). It contributes to metabolic health through improved glucose homeostasis, insulin sensitivity, and protection against obesity-related dysfunction. Due to this, there is growing interest in developing physiologically relevant human *in vitro* models to study its biology. In this thesis, a novel 3D spheroid model of human BAT was established using primary human brown adipocytes. To assess whether the model reproduces key BAT features, differentiated (DIFF) brown adipose (BA) spheroids were compared with undifferentiated (UND) BA spheroids and DIFF white adipose (WA) spheroids using BAT and white adipose tissue (WAT) samples from three patients.

Immunofluorescence staining for UCP1, Perilipin-1 (PLIN1), and CD31 were combined with a viability assay and transmission electron microscopy (TEM). Quantitative image analysis was performed in Fiji/ImageJ using a reproducible pipeline.

The results showed that DIFF BA spheroids displayed BA-like features compared with UND BA spheroids, with an average UCP1-positive area fraction of 27.8% and 0% respectively. In contrast, WA spheroids showed low UCP1 signal, while UND BA spheroids showed none. TEM confirmed abundant mitochondria and multilocular lipid droplet morphology in DIFF BA spheroids. For viability assessment, an average percentage of 91.6% was quantified for BA spheroids, further supporting structural stability. CD31 positivity was low in all groups, as expected due to the absence of endothelial cells.

Overall, this work establishes a primary human 3D BA spheroid model that captures structural and phenotypic hallmarks of BAT and provides a strong foundation for translational studies.

Keywords: Brown Adipose Tissue, Thermogenesis, Uncoupling Protein 1, Spheroids, Image analysis, 3D-Cell Culture Techniques.

List of abbreviations

- ASCs – Adipose-Derived Stem/Stromal Cells.
- AT – Adipose Tissue
- BA – Brown Adipocytes
- BAT – Brown Adipose Tissue
- BMI – Body Mass Index
- cAMP – Cyclic Adenosine Monophosphate
- DIFF – Differentiated
- DPBS – Dulbecco's Phosphate Buffered Saline
- ECM – Extra-Cellular Matrix
- EM – Electron Microscopy
- PET-CT – Positron Emission Tomography-Computed Tomography
- PI – Propidium Iodide
- PLIN 1 – Perilipin-1
- ROI – Region of Interest
- Sc WAT – Subcutaneous White Adipose Tissue
- SVF – Stromal Vascular Fraction
- TEM – Transmission Electron Microscopy
- UCP1 – Uncoupling Protein 1
- UND – Undifferentiated
- WA – White Adipocytes
- WAT – White Adipose Tissue

Table of Contents

List of Figures

List of Tables

1. Literature Overview

1.1. Obesity and Cardiometabolic health worldwide

The 2024 World Obesity Report projects that by 2030, half of the world's adult population will be living with overweight or obesity *(Powis et al., 2025)*. Excess adiposity not only substantially elevates the risk of metabolic disorders, cardiovascular diseases and several cancers but also diminishes quality of life and increases socioeconomic burden *(de Gonzalez et al., 2010; Prospective Studies Collaborations, 2009)*. One of the major causes of obesity is an imbalance between energy intake and expenditure, which primarily depends on **adipose tissue (AT)** *(Luo et al., 2025)*. AT, commonly referred to as "fat," is no longer regarded as merely a passive energy store but is recognized as an active organ that plays essential roles in regulating food intake, energy homeostasis, insulin sensitivity, immune responses, and thermoregulation *(Sakers et al., 2022; Scherer, 2019)*.

1.2. The Adipose Tissue and its Morphology

There are three different types of AT based on their morphological, biochemical and physiological attributes which are very well described by various studies *(Pilkington et al., 2021; Luo et al., 2025; Escudero et al., 2023a; Strobel et al., 2021)*.

The **white adipose tissue (WAT)** adipocytes are attributed by low mitochondria number, single-large lipid droplets and limited cytoplasm *(Ha et al., 2026)* **whereas brown adipose tissue (BAT)** is known to have abundant mitochondria and numerous small lipid droplets in the adipocytes, and heavy vascularization *(Scheele and Wolfrum, 2020; Luo et al., 2025; Pilkington et al., 2021)*. In fact, **brown adipocytes (BA)** are regarded as having one of the highest mitochondrial densities among mammalian tissues *(Kajimura, 2025)*. A further difference between the two adipose tissue types is their contrasting roles in energy metabolism. WAT primarily functions in long-term energy storage by accumulating lipids, whereas BAT is specialized for energy dissipation, converting chemical energy into heat through thermogenesis *(Ha et al., 2026)*. Besides white and brown adipocytes, beige (or brite) adipocytes represent an inducible thermogenic cell type that emerges within WAT and BAT. Through a process known as beiging or

browning, white adipocytes (WA) or their progenitors can acquire brown-like, thermogenic properties in response to stimuli such as cold exposure or hormonal signals. Beige adipocytes share several defining features with BA, including multilocular lipid droplets, a mitochondria-rich cytoplasm, and the capacity to express thermogenic genes such as *UCP1*. However, unlike classical BA, which arise during embryonic development and are located in dedicated brown fat depots, beige adipocytes emerge postnatally within WAT depots in response to specific stimuli such as cold exposure or β-adrenergic activation (*Wu et al., 2013; Harms and Seale, 2013*).

1.2.1. Brown Adipose Tissue and its Metabolic Importance

To counter severe obesity, surgical interventions are used but these are very invasive and can infer risks and complications *(Kraljević et al., 2025; Mihoko et al., 2020; Kajsa et al., 2020)*. To address this challenge, a feasible approach is to increase the body's energy expenditure by activating **uncoupling protein 1(UCP1)** *(Quan et al., 2024)* which is the canonical feature of BAT *(Pilkington et al., 2021)*. UCP1 is a protein found in the inner-mitochondrial membrane of BA and is essential for non-shivering thermogenesis. Its presence is important to distinguish between thermogenic active BA and WA, and it is commonly used as an indicator of brown adipocyte identity and thermogenic potential. Instead of driving ATP synthesis, the electrochemical energy generated by substrate oxidation is released as heat, thereby uncoupling oxidative phosphorylation from ATP production *(Fedorenko et al., 2012; Zhang et al., 2020)*. This process is enabled by the exceptionally high mitochondrial content of brown adipocytes which helps them rapidly oxidize glucose and fatty acids to fuel heat production, linking thermogenesis directly to whole-body energy expenditure and substrate clearance. Collectively, the activation of BAT and UCP1-mediated thermogenesis (**Fig. 1**) positions BAT as one of the regulators of systemic metabolic homeostasis and an attractive target for combating obesity and related metabolic diseases.

For many years, BAT was believed to be absent or physiologically irrelevant in adult humans. This view was challenged by a series of landmark studies, including work led by Kirsi Virtanen, *(Virtanen et al., 2009)* and several independent research groups *(Cypess et al., 2009; Saito et al., 2009; van Marken Lichtenbelt et al., 2009)*, which

demonstrated metabolically active BAT in adults by using [^{18}F]**FDG Positron Emission Tomography–Computed Tomography (PET-CT).** Beyond confirming the presence of BAT *in vivo*, PET-CT also became important for localizing active depots, especially in the supraclavicular region, which in turn enabled targeted biopsy collection for further characterization of human BAT(*Lee et al., 2011*).

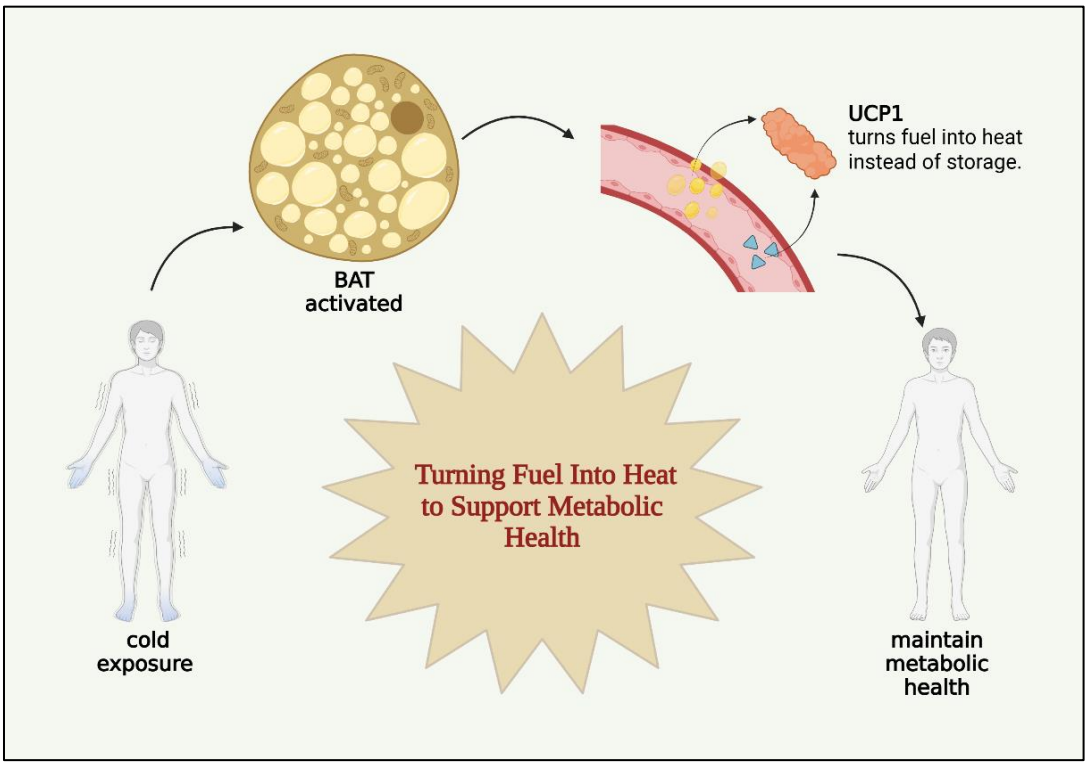

Figure 1. Schematic overview of brown adipose tissue activation and its metabolic role. *Cold exposure activates brown adipose tissue (BAT), promoting the uptake of glucose and lipids (fuel) from the circulation. These substrates are then utilized through UCP1-mediated thermogenesis, in which chemical energy is dissipated as heat rather than stored, thereby supporting energy expenditure and metabolic health.*

These studies, along with others *(Berry et al., 2017; Silva and Amato, 2022)* also demonstrated that in adult humans, BAT mass has been negatively correlated with obesity and aging. Ever since then, BAT has gained a lot of popularity contributing to a rapid expansion of the field, with annual research output increasing from fewer than 200 publications in 2006 to nearly 1,000 publications by 2022 *(Cypess et al., 2025)*. Collectively, rodent *(Feldmann et al., 2009; Stanford et al., 2012)* and human *(Lee et al., 2010; Jacene et al., 2011; Ouellet et al., 2011)* studies provide strong evidence that BAT plays an important role in whole body homeostasis and overall metabolic health.

Another protein marker associated with BAT is CD31 which is also known as **platelet endothelial cell adhesion molecule-1 (PECAM-1).** It is highly expressed at endothelial cell-cell junctions and is commonly used as an endothelial marker (*Lertkiatmongkol et al., 2016*). Its presence in BAT indicates vascularization and this dense capillary network supports oxygen and nutrient delivery, substrate exchange, and heat distribution during thermogenesis (Lee et al., 2023). Vascularization is functionally important for BAT, as BAT-specific VEGF-A expression has been shown to upregulate thermogenic markers such as UCP1, thereby supporting thermogenic activity(*Sun et al., 2014*).

1.3.3D AT Models and their Relevance

BAT is found in supraclavicular regions in human adults but is very scarce (roughly < 10% of all body fat) as compared to WAT *(Pilkington et al., 2021)*. Additionally, there is also lack of relevant human 3D models that can be used for testing drugs and chemicals to stimulate BAT *(Yao Xi and Dani, 2022)*. Such models are very popular nowadays as spheroids and organoids. Both represent commonly used 3D culture systems with distinct levels of biological complexity. Spheroids are relatively simple aggregates of cells that self-assemble through cell-cell interactions and are straightforward to generate, making them practical models for controlled experimental studies and screening applications. Organoids, in contrast, are more complex self-organizing 3D structures, usually derived from stem cells or tissue-specific progenitor cells. Unlike spheroids, organoids can develop more tissue-like organization, contain multiple cell types, and partially mimic the architecture and function of the tissue of origin. Therefore, spheroids mainly represent 3D cellular aggregates, whereas organoids aim to reproduce organ-like features at a higher level of biological complexity.*(Liu et al., 2024; Gunti et al., 2021)*. With respect to AT, they can act as a powerful tool for studying their development, progression and interaction with the surrounding niche. Moreover, it can also aid in understanding their role in obesity and can accelerate medical research, drug discovery, and toxicity testing *(Bredenoord et al., 2017).* Compared with two-dimensional cultures, 3D aggregates are better able to preserve cell viability and differentiation potential. They are also shown to enhance paracrine signaling (adipokines/batokines), better mimic **extra cellular matrix**

(ECM) mechanics, and allow tissue-level readouts (e.g., vascular-like networks, lipid droplet architecture) *(Liu et al., 2024; Mandl et al., 2022; Robledo et al., 2023)*.

So far, several 3D adipose culture systems have been developed, but their origins make clear that the field still lacks a 3D spheroid model generated directly from primary human BA. The reason being limited access to human BAT and the technical difficulty of culturing mature adipocytes as they are fragile, and lipid-rich leading to difficulty in handling. *, Davidsen et al., 2024* established vascularized adipose spheroids from the **stromal vascular fraction (SVF)** of mouse inguinal WAT, using ultra-low attachment aggregation followed by ECM embedding, thereby creating a beige-competent murine model. Similarly, *Robledo et al., 2023* produced adipose spheroids from the SVF of newborn mouse interscapular BAT, using hanging-drop and low-adhesion approaches to obtain structurally complex, leptin-secreting organoids. On the human side, WAT spheroids have been created by *Mandl et al., 2022* using freshly isolated adipose-derived Stem Cells (ASCs) from subcutaneous WAT (Sc WAT) and *Escudero et al., 2023* using SVF of human WAT. Moreover, generation of BA 2D *in vitro* models has been reported by *Shinoda et al., 2015* and *(Xue et al., 2015)* from SVF derived from adult human neck-fat that showed UCP1 expression and thermogenic features. These studies represent important advances in the field. However, they were derived from conventional monolayer culture and immortalized or clonally expanded progenitor populations rather than a 3D patient-derived tissue model. This is an important limitation, as adipocyte maintenance, morphology, and function are strongly influenced by 3D organization and the surrounding microenvironment. Therefore, despite all these advances, to our best knowledge there is still no bona fide 3D model built directly from primary human BA.

1.4. Microscopy and Image Analysis of 3D Models

The characterization of 3D models relies heavily on imaging approaches that preserve tissue architecture while still allowing detailed structural assessment. Among these, confocal microscopy has become the main workhorse, the reason being its ability to provide images with very good signal to noise ratio by filtering out of focus light through a pinhole (**Fig.2**).

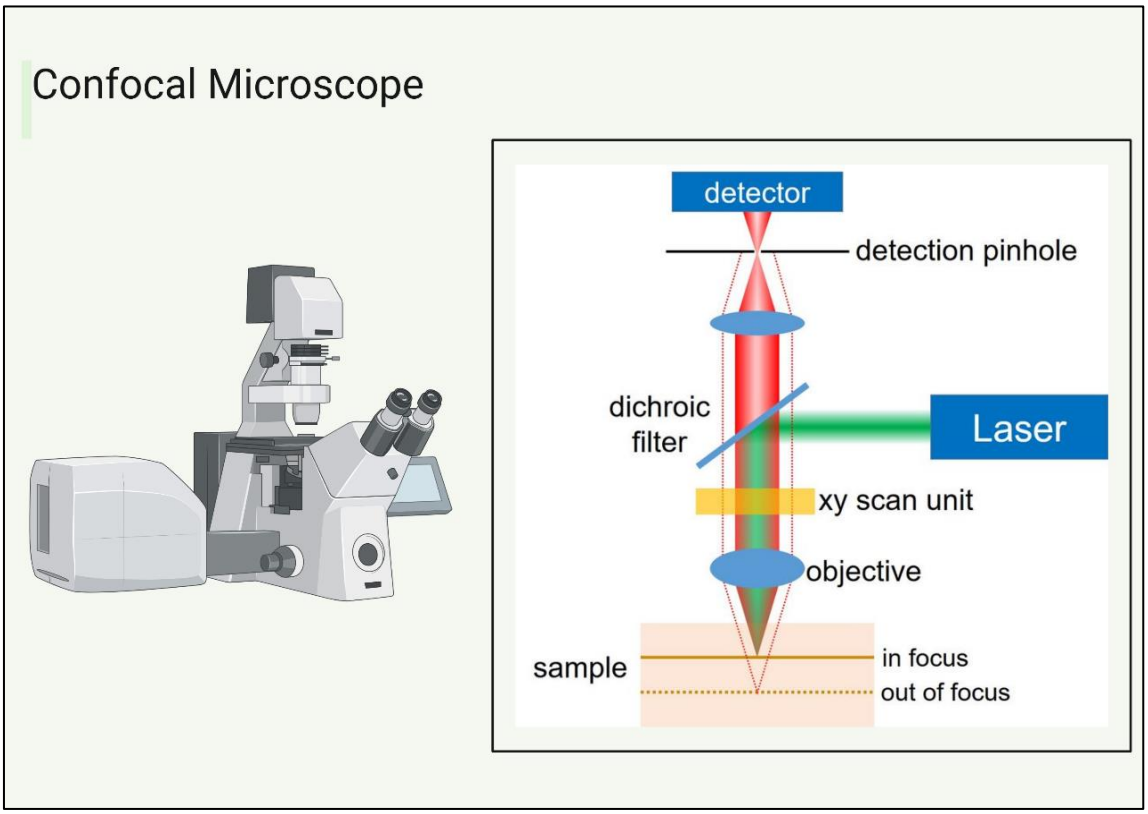

Figure 2. Confocal microscope and simplified schematic of the imaging principle.
Schematic showing the basic optical path in confocal laser scanning microscopy, in which laser excitation is focused onto the sample and emitted fluorescence.

This allows thick and structurally complex samples to be imaged with improved contrast and resolution compared with conventional widefield fluorescence microscopy. In addition, the acquisition of serial optical sections enables visualization of different depths within the sample and allows reconstruction of its 3D organization without the need for physical sectioning.

This particularly facilitates imaging of lipid-laden tissues like BAT as large lipid droplets contribute to light scattering and can reduce image clarity. Moreover, BAT also exhibits

autofluorescence that interferes with signal detection *(Martinez-Santibañez et al., 2014)*. Confocal microscopy helps to mitigate these limitations by improving contrast and reducing background signal, thereby enabling clearer visualization of fluorescent markers within structurally complex adipose samples. For this reason, confocal microscopy is especially well suited for assessing marker localization, adipocyte morphology, and the spatial arrangement of cells within 3D BAT models.

It is well known that fluorescence microscopy does not resolve ultrastructural details. To overcome this, confocal imaging is often paired with **electron microscopy (EM)**. **Transmission electron microscopy (TEM)** provides structural information beyond the resolution of routine fluorescence imaging. Its principle is based on the transmission of an electron beam through ultrathin sections of the specimen, where differences in electron density generate contrast and reveal fine intracellular structures at very high resolution (**Fig.3**). This makes TEM particularly valuable for visualizing organelles and subcellular architecture that cannot be resolved by light microscopy.

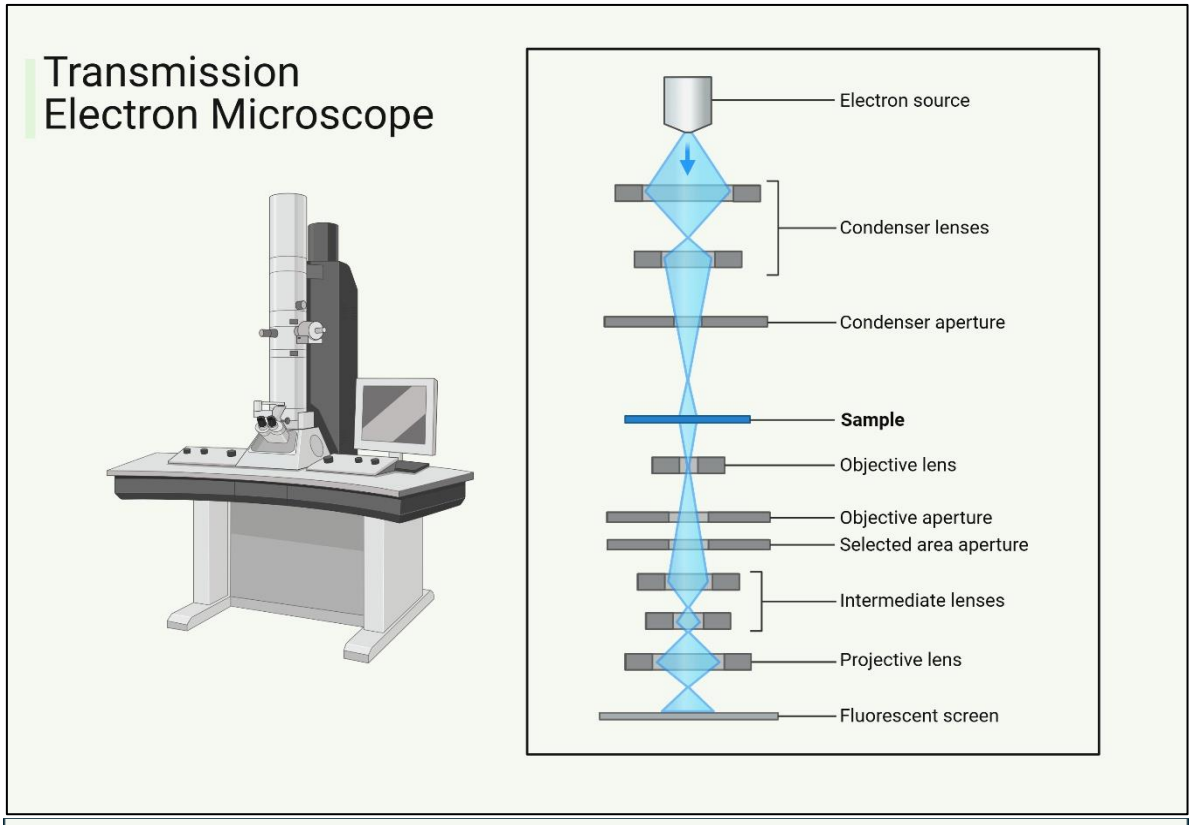

Figure 3. Transmission electron microscope and simplified schematic of the TEM imaging principle. *Schematic showing the basic principle of transmission electron microscopy, in which an electron beam passes through an ultrathin specimen and contrast is generated according to its electron density, enabling visualization of internal ultrastructural details at high resolution.*

Multiple studies like *Herbers et al., 2022; Robledo et al., 2023; Shen et al., 2021 and Yao Xi and Dani, 2022* combined confocal microscopy with EM to confirm the complex cellular organization and ultrastructure of adipose spheroids.

As spheroids increase in size, imaging of the inner region becomes additionally challenging because of problems such as light scattering and signal attenuation increases with growing depth. To overcome this limitation, optical clearing has become a salient component of 3D model imaging workflows, particularly for larger and more structurally complex samples. In AT research, several clearing strategies have been adopted for this purpose. *(Chi et al., 2018)* developed Adipo-Clear, a method specifically adapted for lipid-rich adipose tissue to enable comprehensive 3D visualization while preserving tissue morphology. Similarly, *Yao Xi and Dani, 2022* reported a workflow in which whole adipospheres were fixed, immunostained, cleared with **BABB (Benzoic Acid Benzyl Benzoate)** and then imaged to visualize their internal organization. More recently, *Escudero et al., 2023* incorporated a clearing step with Scale S4 solution before confocal imaging in human beige adipose organoids, further illustrating how closely clearing is linked to the analysis of larger and more complex 3D adipose models.

Image analysis is an important tool in AT research because it allows visual observations to be converted into measurable data. In BAT studies, this is especially useful because BA is characterized by multilocular lipid droplets, high mitochondrial content, and UCP1 expressions, which are key features used to distinguish them from WA (Shinde et al., 2021). Quantitative image analysis can therefore be used to assess parameters such as UCP1-positive area, lipid droplet morphology and viability. In 3D adipose models, image analysis is particularly useful because it helps evaluate whether spheroids retain important BAT-like features in a more objective and reproducible way.

Overall, the field has made substantial progress in the generation and characterization of adipose 3D models, supported by advances in microscopy, optical clearing, and image analysis. Most existing models rely on murine tissue, WAT derived SVF, adipose stromal cells or progenitor-based systems, all of which are valuable but do not fully reproduce the mature state of human BAT. This limitation is important because murine BAT does not entirely mirror human BAT. In addition, primary mature adipocytes offer a closer representation of the *in vivo* state, with better preservation of endogenous cellular

identity, depot-specific gene expression in culture and donor-linked biological variation. The absence of such a system represents a clear methodological and biological gap in the study of human BAT. Therefore, the present thesis aimed to establish and characterize a 3D spheroid model derived from primary human BA.

2. Aims and Hypothesis

The overall aim of this thesis is to establish and validate a fully functional BA spheroid model derived from the isolated SVF from BAT. Since spheroid formation alone is insufficient to demonstrate physiological relevance, the model will be characterized comprehensively at structural, phenotypical, and functional levels to determine whether it replicates key features of human BAT *in vitro*.

To address this aim, the study is guided by the following specific objectives:

1. To **generate BAT spheroids** from primary human BAT pre-adipocytes and characterize them by immunofluorescence staining for markers including UCP1, **perilipin 1(PLIN1**), and CD31 coupled with **transmission electron microscopy (TEM)** to better understand the ultrastructure.
2. To **determine spheroid viability using propidium iodide (PI)** and calcein staining.
3. To **develop a reproducible image analysis pipeline** that enables robust quantification of the above-mentioned markers that may serve as a methodological framework for future studies.

The hypothesis of this thesis was that SVF cells isolated from human BAT can be used to generate a stable, viable, and physiologically relevant 3D BA spheroid model. It was expected that, after differentiation, BA spheroids would show key BAT features, including multilocular lipid droplet morphology, abundant mitochondria, and expression of characteristic markers such as UCP1. In addition to these structural and molecular features, the spheroids were expected to remain viable under the developed culture conditions. Furthermore, BA **differentiated (DIFF)** spheroids were hypothesized to show clear differences compared with BA **undifferentiated (UND)** and WA DIFF spheroids.

3. Materials and Methods

The materials and methods used in this study are described in detail in the following sections. These include experimental procedures, sample preparation steps, reagents, equipment, and analytical approaches applied during the study. A complete list of all reagents, chemicals, equipment, software and other materials used is provided in the supplementary material in **Appendix 1**.

3.1.Study design and participants

Samples for following experiments were collected from lean and healthy winter swimmers (BMI<25 kg/m2, age within 18-41 years, attending at least 2 times/week to ice swimming) as a part of MOTORBAT study (ClinicalTrials.gov ID: NCT05468151).

Subject recruitment was done via electronic media advertisements and leaflets. The exclusion criteria were based on the inability to undergo PET/CT scanning, pregnancy, smoking, hypertension, hypo/hyperthyroidism, diabetes mellitus, abnormal cardiovascular status, and any other condition that could influence the study outcomes. Ethical considerations were observed and reviewed throughout the study. Moreover, all participants provided written informed consent prior to any study-related procedures. The recruitment, collection, assessments and procedures were all performed in Turku, Finland.

Out of the recruited patients, three were selected based on their BAT glucose uptake rate which was used as a marker of BAT metabolic activity. This uptake was measured using PET/CT with the radiotracer [^{18}F] fluorodeoxyglucose ([^{18}F] FDG). They have the IDs: 117S (male, BMI 24.7 kg/m², age 34, passage 5), 123S (male, BMI 25.8 kg/m², age 34, passage 5), and 124S (female, BMI 20.8 kg/m², age 41, passage 5). Initially, the participants were exposed to mild cold using cooling blankets to stimulate BAT activity. After 100 min of cold exposure, a [^{18}F] FDG-PET/CT scan was performed to quantify BAT glucose uptake. Participants exhibiting higher levels and hence elevated metabolic activity were selected. A separate appointment was scheduled for the collection of the BAT and scWAT samples from these patients by an experienced plastic surgeon at the Turku University Hospital. The procedure was performed under local anesthesia. The surgeon located the metabolically active BAT depots in the supraclavicular area using

[^{18}F] FDG-PET/CT scans. First, scWAT samples were taken from superficial neck AT, followed by dissection to locate the precise BAT depot, from which 1-2 g of BAT tissue was usually collected. BAT and scWAT samples were transported on ice to the Medicity laboratory in DMEM/F12 medium, supplemented with 1% penicillin-streptomycin. After removal of connective tissue and lymph nodes, samples were minced and digested with collagenase II at 37 °C. The resulting cell suspension was filtered, centrifuged, and washed, yielding a mixed stromal vascular fraction containing adipose progenitor cells together with other cell types, such as immune and endothelial cells. Cells were seeded into T25 flasks in human preadipocyte growth medium (DMEM/F12 supplemented with 1% Pan/Bio (prepared with 3.3 mM Pantothenate 1.7 mM biotin solution), 1% Penicillin/Streptomycin solution, 5% human serum and 0.015% FGF-1 stock) and expanded under standard culture conditions until 80–90% confluency, with medium changes every 2 days. After further expansion, cells were cryopreserved at 1×10^6 cells/mL in medium containing 10% DMSO and 90% human serum using controlled-rate freezing before transferring to long-term storage at −150 °C.

3.2. Generation of primary 3D human brown adipose spheroids

All the experiments were conducted individually and independently, spanning approximately 2 months each. The BA and WA spheroids for each patient were generated almost simultaneously.

To begin the experiment, an aliquot of the cryopreserved BA and WA SVF cell suspension was thawed, washed in HPG medium, and seeded into T25 flasks. They were allowed to culture (passage 3/P3) until reaching a confluency of 80-90%. After this, they were passaged to a T75 flask (passage 4/P4) until 80-90% confluency was reached and then split to three T75 cell culture flasks (passage 5/P5). When that confluency was achieved again the cells are considered ready for seeding (**Fig.4**).

For seeding, 40,000 cells were seeded day-1 (D-1) in 200 µL of seeding medium, which consisted of DMEM/F12 supplemented with 0.4% P/S, 0.2% Amphotericin B, 1% Pan/Bio and 0.1% insulin solution. The 96 well ultra-low attachment plates were employed for generations of the 3D spheroids as they promote natural aggregation and self-assembly based on cell-cell interactions, rather than adhering to the substrate.

The following day at D0 a subset of 18 spheroids for BA and WA each, was collected. These were UND spheroids. Out of these 10 were cryopreserved in OCT blocks at -80 ºC until further analysis, 8 were utilized for TEM. For the rest of the spheroids, separate induction media were prepared for BA and WA spheroids, to initiate adipogenesis, which means the phase during which preadipocytes differentiate into mature cells and start accumulating more lipids.

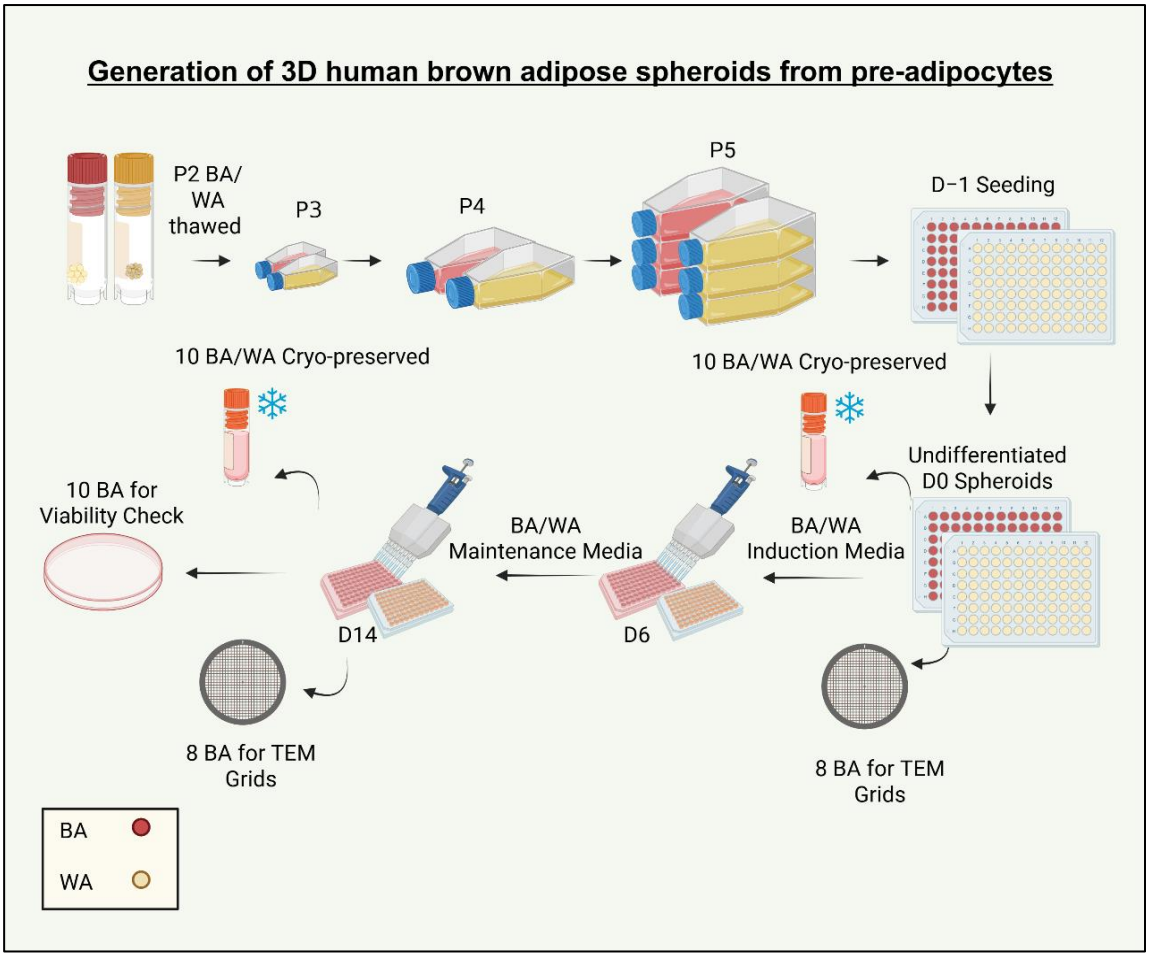

Figure 4. Generation, differentiation, and sampling of 3D human adipose spheroids. *Cryopreserved SVF preadipocytes from BA and white WA adipose tissue were thawed at passage 2 (P2) and expanded to passage 5 (P5) prior to seeding. On day −1 (D−1), cells were seeded into ULA 96-well plates to promote self-aggregation and spheroid formation. On day 0 (D0), UND spheroids were collected, including 18 BA spheroids (allocated to cryopreservation in OCT at −80 °C and TEM processing) and 10 WA spheroids, which were collected exclusively for cryopreservation. Remaining spheroids were DIFF using BA or WA specific induction media (D0–D6, medium change every 2 days) followed by maintenance media (D6–D14, medium change every 2 days) to support lipid accumulation. On D14, spheroids were harvested for downstream applications: WA spheroids were again collected only for cryopreservation (n=10), while BA spheroids were collected for additional endpoints including TEM and viability assessment.* ***Abbreviations****: BA, brown adipose; WA, white adipose; SVF, stromal vascular fraction; ULA, ultra-low attachment; OCT, optimal cutting temperature compound; TEM, transmission electron microscopy.*

White induction media consisted of DMEM/F12 with 0.4% Penicillin/Streptomycin solution, 0.2% Amphotericin B, 1% Pan/Bio, 1.8 μM Insulin, 1 μM Dexamethasone, 125 mM Indomethacin and 0.5% Intralipid. Brown induction media was composed of DMEM/F12 with 0.4% Penicillin/Streptomycin solution, 0.2% Amphotericin B, 1% Pan/Bio, 1.8 μM Insulin, 1 μM Dexamethasone, 1 μM Rosiglitazone and 120 nM T3. The plates were left in the incubator at 37 ºC and 5 % CO2 for 6 days with media change after every two days (**Fig.4**).

On D6, the induction media was replaced with maintenance media, to initiate growth and accumulation of lipid droplets. The maintenance media for BA was composed of DMEM/F12 with 0.4% Penicillin/Streptomycin solution, 0.2% Amphotericin B, 1% Pan/Bio, 1.8 μM Insulin, 1 μM Rosiglitazone and 120 nM T3 whereas for the WA, 0.5% Intralipid was used instead of 1 μM Rosiglitazone. Media was replenished every two days until D14 (**Fig.4**).

Eventually, on D14, 10 spheroids each for BA and WA were collected and cryopreserved in OCT cryoblocks at -80ºC until further experimentation, 8 of the DIFF BA were utilized for TEM and 10 were used to assess viability of the spheroids (**Fig.4**).

3.3. Viability checks with Propidium Iodide (PI) live staining

A subset of 8 BA and WA spheroids was collected at D14 in a petri dish containing **Dulbecco's phosphate buffered saline (DPBS)**. Out of these 4 were transferred to a separate dish and incubated with 70% ethanol for 10 min at RT. This treatment permeabilized the cell membranes and served as a positive control for dead-cell staining. Rest of the protocol is same for the control and experimental spheroids.

The spheroids were washed 3 times with DPBS, with each washing being 5 min long. Next, they were incubated at 37 ºC for 1 h with 10 ug/mL PI prepared by diluting 1 mg/ml stock in phenol-red free, serum free cell culture media. From this step onwards the samples were protected from light. After an hour, PI was removed and the spheroids were washed again, gently with DPBS thrice, 5 min each. For fixation, paraformaldehyde (PFA) 4% in PBS was added to the dishes and left for 20 min. The spheroids were washed again with DPBS three times and then permeabilized with 0.1% Triton-X 100 for 10 min at RT. This was followed by two PBS washings, 5 min each and incubation with 2 ug/ml

Hoechst for 10 min at RT. Subsequently, three long washes with DPBS were done stretching to 30 min each on a Standard Analog Shaker by VWR ™ (speed 5) to ensure all residues were removed and then incubated in clearing solution for 48 h at RT. For optical clearing, Scale S4 clearing solution was used, which was prepared in advance by mixing 40% D-sorbitol, 10% Glycerol, 24.024 g Urea, 0.2% Triton-X 100 and 15% DMSO together and toping up with MilliQ water till 100 Ml. This solution was left for 16 h at 37 ºC until ready for use. The prepared live spheroid samples were then imaged with a confocal microscope.

3.4.Sample preparation for transmission electron microscopy (TEM)

For TEM 8 BA spheroids were collected at D0 and D14 for ultrastructure analysis.

The spheroids were collected in Petri dishes and washed with PBS two times, 5 min each. Then 3 mL of the prepared fixatives (**Table 1**) were added to specially labelled tubes along with the spheroids and left to incubate for the designated times of 6 h and 24 h respectively. Afterwards the fixatives were carefully discarded and 3 mL of 0.1M phosphate buffer (pH 7.4) was added to each tube. The samples were immediately transported to electron microscopy core facility for further processing and grid preparation.

Table 1.Fixatives used to fix the BA spheroids.
4 spheroids were fixed per condition/experiment for two incubation times of 6 h and 24 h respectively.

Fixative	Reagents
2 % GA + 2 % PFA	5520 ul 2% PFA, 0.1M PB and 480 ul 25 % GA
2% GA	5520 ul 0.1M PB and 480 ul 25 % GA

3.5. Preparation and Immunostaining of Spheroid Cryo-sections

Cryo-sections were prepared and immunostained to verify the presence of selected cell types within the spheroids. Detailed materials and methods are described in the following subsections.

3.5.1. Cryo-sectioning of spheroids

Cryo-sections were cut using Leica CM3050 S cryostat at the object temperature of -25 ºC. The 9 um thick sections were collected on microscope slides and kept at -20 ºC, labelled until the staining.

3.5.2. Immunostaining of Cryo-sections

To begin with, cryo-sections were taken out of the freezer and allowed to thaw for 15 min. Sections were selected carefully after observing under the Olympus Microscope CX21 Binocular Head (10x/0.25 objective) for their quality, intactness and roundness.

The sections were then washed in PBS for 2 min. After this the sections were fixed with ice cold 99.9% Methanol in a glass jar, on an ice block, for exactly 5 min as longer incubation can break mitochondria. This was followed by two PBS washes, 2 min each. Next was fixation with ice cold 99.8% Acetone in a glass jar on an ice block for 1 min. The sections were washed again twice with PBS after which they were permeabilized with 0.1% Triton-X 100 for 5 min. Washing was done again, and the slides were placed in a plastic box with the spheroids circled with a hydrophobic pen to retain the stains later. Once the pen was dried, 40 ul of Blocking Solution (3% BSA and 0.2% Tween20 solution) was added to each section and incubated for an hour (**Fig.5**).

After 60 min, the blocking solution was removed, and sections were washed with PBS for 2 min. The slides were placed in a plastic box and 40 ul of the primary antibody (details of the antibodies used and their concentrations can be seen in table 2) was added to all sections except the unstained controls, after which they were left at 4 ºC overnight. The unstained controls were incubated with just washing buffer.

zNext day, the sections were washed in washing buffer (WB) (1% BSA and 0.1% Tween20 solution) twice for 5 min each. Then the sections were incubated with 40 ul of the secondary antibody, (**Table 2A and B**) for an hour.

Table 2. List of antibodies used in the study.
Secondary antibodies are listed with host species (raised in), fluorophore, supplier, catalogue number, and working dilution. Goat anti-mouse IgG Alexa Fluor 568 (A11004; 1:1000) was used to detect the mouse primary antibodies UCP1 and CD31, while goat anti-rabbit IgG Alexa Fluor 750 (A21039; 1:200) was used to detect the rabbit primary antibody PLIN1.

A

PRIMARY ANTIBODIES

Target	Host	Clonality	Supplier	Cat. no.	Dilution
UCP1	Mouse	Monoclonal	R&D	MAB6158	1:100
PLIN1	Rabbit	Polyclonal	ThermoFisher	PA5-72921	1:500
CD31	Mouse	Monoclonal	Bio-Rad	MCA1738	1:100

B

SECONDARY ANTIBODIES

Antibody (anti-x)	Host (raised in)	Fluorophore	Supplier	Cat. no.	Dilution
anti-mouse IgG	Goat	Alexa Fluor 568	Invitrogen by ThermoFisher	A11004	1:1000
anti-rabbit IgG	Goat	Alexa Fluor 750	Invitrogen by ThermoFisher	A21039	1:200

After this, the sections were washed again but this time thrice, 5 min each to ensure no unbound stain is left (**Fig.5**).

Due to high intrinsic autofluorescence of adipose tissue, Vector® TrueVIEW® Autofluorescence Quenching Kit was used as an additional step in UCP1 and PLIN1 staining to improve detection of true immunofluorescence signals. It was prepared according to product instructions and left on the sections for 5 min, after which they were washed with PBS for 5 min (**Fig.5**).

For nuclear counterstaining, sections were incubated with 40 µL of 5 ug/ml DAPI for 10 min, followed by two washes in PBS for 5 min each using glass staining jars. Finally, the slides were covered with VECTASHIELD Vibrance® Antifade Mounting Medium by pipetting it on top of the sections and adding a thin cover slip. After this they were left to dry, protected from light, at RT for 1-2 hours (**Fig.5**). The slides were then stored at 4 ºC until microscopy.

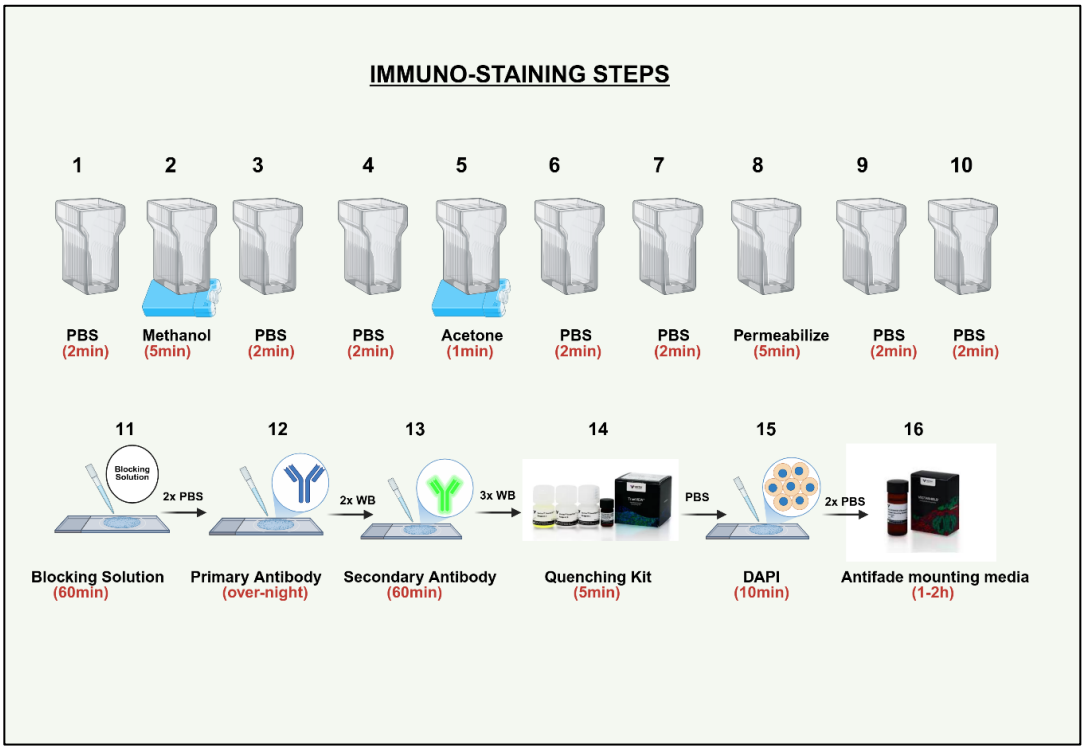

Figure 5.Immunostaining workflow for cryosections.
Sections were washed in PBS and fixed using methanol (5 min) and acetone (1 min), followed by PBS washes. Samples were then permeabilized (5 min) and washed in PBS before blocking (60 min). Sections were incubated with primary antibodies overnight and washed prior to secondary antibody incubation (60 min). Autofluorescence was reduced using a quenching kit (5 min), followed by nuclear staining with DAPI (10 min) and mounting in antifade medium (1–2 h). Wash steps (PBS/WB) are indicated in the schematic.

3.6. Microscopy

Fluorescence and ultrastructural imaging were performed using confocal microscopy and TEM, respectively. Confocal microscopy was used to image immunofluorescence-stained spheroid cryosections and to perform live imaging for viability assessment. Transmission electron microscopy was used to gain in depth information about the ultrastructure of the spheroids, including features such as mitochondrial abundance, lipid droplet morphology, and cellular organization.

Together, these complementary imaging approaches provided both phenotypic and structural characterization of the spheroids. All imaging was carried out under standardized and consistent conditions; the image quality was assessed prior to analysis.

3.6.1. Confocal Microscopy

All stained spheroid cryosections were imaged using a Leica Stellaris 8 Falcon FLIM microscope equipped with FCS and a resonant scanner. Fluorescence imaging was performed at 20× magnification using a Leica HC PL APO CS2 20×/0.75 objective. UCP1 and CD31 images were acquired using the air objective at 0.75× zoom. A pinhole setting of 1 AU was used, corresponding to 56 µm.

For viability imaging, PI-stained samples were acquired at the same magnification and zoom using a Leica HC PL APO CS2 20×/0.75 immersion objective with water as the immersion medium, refractive index 1.33, and a pinhole setting of 1 AU, corresponding to 56 µm. Imaging parameters were kept constant within each staining protocol to ensure comparability between samples and to minimize technical variation between image acquisitions.

3.6.2. Transmission Electron Microscopy

EM was performed using a JEM-1400 Plus TEM, operated at an accelerating voltage of 120 kV, with a resolution of 0.38 nm. Ultrathin tissue sections of approximately 50 nm were prepared using an ultramicrotome and collected on 1 mm diameter, 300-mesh nickel grids. The sections were subsequently contrasted with lead citrate before imaging.

3.7. Image Analysis

For analyzing the images software ImageJ/FIJI was used. The pipelines were developed for each marker, and special care was taken to get most information out of the images. All fluorescence images were analyzed using a standardized workflow to ensure consistency across samples and to minimize user dependent bias. Prior to analysis, each image was subjected to quality control, and images were excluded if

they failed to fit in with the predefined criteria. Images were not included in the dataset to be analyzed if they had saturated signal, truncated fields of view, out-of-focus acquisition, unsuccessful nuclear segmentation or imaging artefacts like excessive debris. Any excluded images were documented.

3.7.1. UCP1 Marker

An image analysis pipeline was developed to calculate the fraction of spheroid area positive for the marker. This pipeline was termed control-defined threshold-based positivity analysis, because a matched UND negative control was used to define the cut-off value for each patient. The same analysis steps were applied to all images to ensure consistency and reproducibility.

The total spheroid area was defined manually in Fiji using the Freehand Selection Tool based on the DAPI channel. Because the spheroids were tightly packed, the ROI was drawn slightly beyond the nuclear boundary to include the full spheroid area while still following its true outline closely. The same operator performed all ROI selections using the same criteria throughout the analysis. For each image, the ROI overlay was inspected visually before continuing to ensure that the selected area matched the spheroid accurately. As the DAPI signal was relatively dim, contrast was enhanced uniformly by 0.5% across all images, followed by Gaussian blurring (sigma = 1.0), to improve visualization of the spheroid boundary during ROI selection.

For quantification of UCP1-positive area, the same ROI selection workflow was first applied to the matched UND negative control, which was processed in the same staining batch and used to define background signal for that patient. The ROI obtained from the negative-control DAPI channel was then transferred to the corresponding UCP1 channel to measure background, autofluorescence, and non-specific signal within the spheroid area. Based on these measurements, a positivity threshold was defined separately for each patient using the following formula:

$$\boldsymbol{T = mean\ negative\ control + 3(SD\ of\ negative\ control)}$$

The threshold (T) was defined as the mean value of the negative control plus three times its standard deviation. This approach accounts for background signal and its variability, allowing samples exceeding this threshold to be distinguished from negative background with higher confidence and omitting any false-positive signal.

After the threshold had been defined, the same ROI selection procedure was applied to the corresponding experimental images. The predefined threshold value for that patient was then applied as the lower threshold in the UCP1 channel, and Fiji was used to calculate the Area Fraction within the ROI. This value represented the proportion of spheroid area positive for UCP1 relative to the total spheroid area. Area fraction was used to provide an overall estimate of the presence and extent of UCP1 positivity within each spheroid.

All measured values were recorded and stored in an Excel file together with information on experiment, patient number, condition, and replicate. Imaging settings were saved and reapplied in subsequent imaging sessions to maintain consistency across image acquisition. Replicate values for each patient were then averaged to obtain one final percentage of UCP1 positivity per patient.

The same workflow was applied to all experimental groups, including BAT DIFF, BAT UND, WAT DIFF, and WAT UND spheroids, after which the resulting data were compared between groups.

3.7.2. CD31 Marker

For image analysis of CD31 marker, the same control-defined threshold-based positivity analysis pipeline as described for UCP1 was used, except that the CD31 channel was analyzed instead of the UCP1 channel. Briefly, the ROI defined manually on the DAPI channel was transferred to the corresponding CD31 channel, and matched secondary-only controls were used to establish a background-derived positivity threshold for each patient.

This threshold was then applied as the lower threshold for the corresponding experimental images. Pixels with fluorescence intensity above this threshold were classified as CD31-positive, whereas pixel values below it was classified as negative. Fiji was then used to calculate the Area Fraction within the ROI, representing the proportion of spheroid area positive for CD31 relative to the total spheroid area.

All measurements were exported to Excel for further processing together with the relevant sample information, and replicate values were averaged per patient to obtain one final percentage of CD31 positivity. The same workflow was applied to all experimental groups, including BAT DIFF, BAT UND, WAT DIFF, and WAT UND spheroids, after which the resulting data were compared between groups.

3.7.3. Viability assay with Propidium Iodide

Viability was assessed from PI, calcein and DAPI stained confocal z-stacks using a standardized three slice analysis workflow. For each patient, two to three spheroid replicates were imaged together with one ethanol-treated control, which served as a positive control for PI uptake. As full volume 3D quantification was not performed, viability was estimated from three predefined optical sections selected from each spheroid stack in a consistent manner.

This section-based approach was considered appropriate because it preserved positional information across the z-axis and provided a more informative estimate than a maximum-intensity projection, while remaining practical and efficient. The use of representative optical sections is also supported by previous studies in 3D spheroid-type models, in which an optical section through the spheroid center or middle/highest-diameter sections were analyzed when full-volume quantification was not performed (*Kobolak et al., 2020; Zanoni et al., 2016)*.

The optical sections to be analyzed were defined using the DAPI channel. The z-planes containing clearly discernible nuclei, with true nuclear signals,

without interference from noise or debris, were identified as the top and bottom sections of the spheroid, respectively, as shown in **Figure 6.** The middle section was defined as the midpoint between these two positions. This yielded three standardized optical sections per spheroid, referred to as top, middle, and bottom.

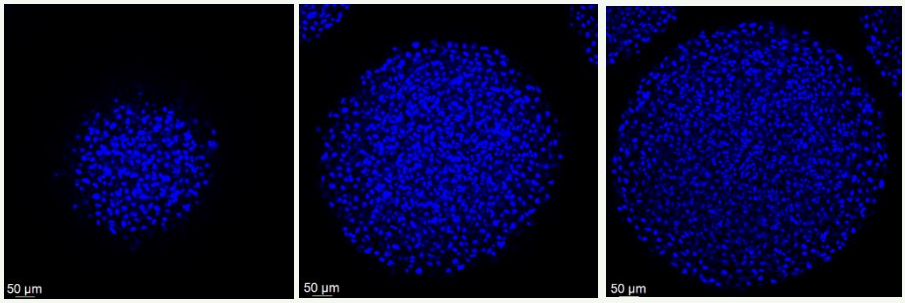

Figure 6. Representative top, middle, and bottom optical sections of a BA differentiated spheroid from patient 117S.
The images show the three DAPI-stained z-planes selected from the confocal z-stack for slice-based viability analysis. The top and bottom sections were defined as the first and last planes containing clearly discernible nuclei, respectively, while the middle section was determined as the midpoint between them.

The same z-positions were subsequently analyzed in the corresponding PI channel to ensure direct comparison between total and dead nuclei within the same regions of the spheroid. Individual optical sections were duplicated from the original z-stack, labelled and subjected to the same processing as defined in the upcoming steps.

The preprocessing started with Gaussian blurring with a sigma of 1.0 to reduce minor image noise and support more stable segmentation. Several automatic thresholding methods were tested, and Otsu thresholding was selected because it provided the clearest and most consistent separation of nuclear signal from background in the present dataset while reducing operator-dependent threshold selection. After thresholding, Watershed was applied only when clearly needed to separate closely adjacent nuclei. The resulting segmentation overlays were inspected visually, and if normal nuclei were split inappropriately, the segmentation was repeated and the watershed result was not accepted.

Quantification was performed in Fiji using Analyze Particles with fixed settings for size and circularity of 15–120 µm² and 0.20–1.00, respectively. The size range was selected to exclude small fluorescent speckles and staining artefacts at the lower end while reducing the inclusion of large irregular objects at the upper end. The circularity range was chosen to accommodate the nuclear morphology observed in the spheroids. These settings were defined after testing different values and verifying the resulting overlays visually. The resulting particle count from the DAPI channel was recorded as the total number of nuclei for each section.

The same analysis workflow was then applied to the corresponding PI images using the identical top, middle, and bottom z-positions, as shown in **Figure 7**.

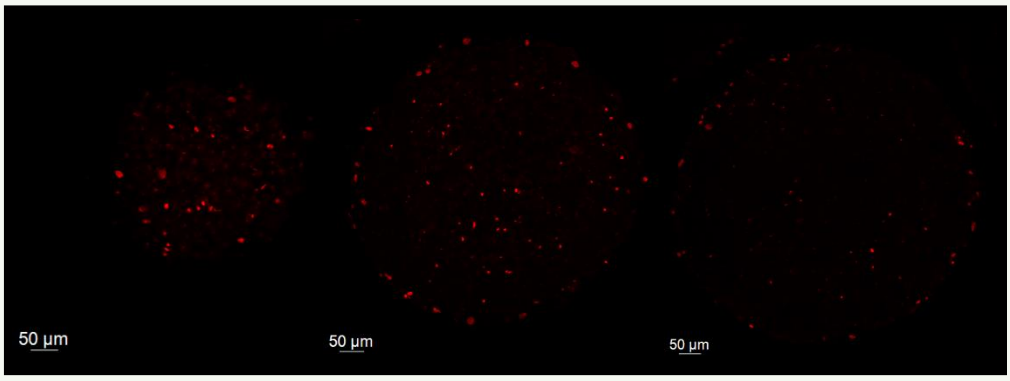

Figure 7.Representative top, middle, and bottom PI-stained optical sections of the same BA differentiated spheroid from patient 117S.
These images correspond to the same z-planes selected in the DAPI channel for slice-based viability analysis and used to quantify PI-positive nuclei, enabling direct comparison with total nuclei within the same spheroid regions.

PI-positive nuclei were quantified using the same particle analysis settings. This was considered appropriate because the ethanol-treated control confirmed that PI-positive nuclei showed a clear, round nuclear morphology comparable to that observed in the DAPI channel. The number of PI-positive nuclei was recorded for each section and used as the estimate of dead cells.

Viability was calculated separately for each of the three analyzed sections using the number of PI-positive nuclei relative to the total nuclei count, according to the following formula:

$$\boldsymbol{Viability}\ (\%) = \mathbf{100}\left(\mathbf{1} - \frac{\boldsymbol{PI\ positive\ nuclei}}{\boldsymbol{total\ nuclei}}\right)$$

The proportion of viable cells is calculated by subtracting the dead-cell fraction from the total cell population. The final viability value for each spheroid was obtained by averaging the viability values from the top, middle, and bottom sections. The same workflow and analysis settings were applied to all analyzed spheroid groups, including DIFF BA and DIFF WA spheroids.

3.7.4. TEM

TEM images were assessed qualitatively by comparing DIFF and UND BA spheroids. No separate quantitative pipeline was developed for TEM data in this study. The evaluation focused on key ultrastructural features, including mitochondrial abundance, lipid droplet morphology, and cellular organization, providing supportive morphological evidence of differentiation-associated changes.

3.8. Statistical Analysis

Given the exploratory nature of the study and the limited number of patient samples (n=3), **the data were interpreted primarily descriptively,** with emphasis on overall trends and consistency across patients, conditions, and replicates. Where applicable, replicate measurements were averaged to obtain one final value per patient for each condition, and the results are presented as mean values or mean ± standard deviation, as specified in the corresponding figure or text. Graphs were prepared using **Microsoft Power BI,** and all figures were created by the author using **Bio Render** unless otherwise stated.

4. Results

To characterize the developed human BA spheroid model, DIFF and UND BA spheroids were compared using immunofluorescence staining, viability assay, and TEM. Each marker was selected to assess a specific feature of the spheroid phenotype. UCP1 was used to evaluate thermogenic BA identity, while PLIN1 staining was used mainly for visualization of lipid droplet organization and adipocyte-like morphology. CD31 was included to assess if the spheroids had vascularization. Viability staining was performed to determine whether the spheroids remained biologically maintained after differentiation, and TEM was used to visually assess ultrastructural features such as mitochondrial abundance, lipid droplet morphology, and cellular organization.

4.1. UCP1 Marker

UCP1 staining showed a clear difference between UND and DIFF BA spheroids (**Fig. 8**). In representative images from patient 117S, BA DIFF spheroids showed detectable UCP1 signal together with clear PLIN1 staining, whereas BA UND spheroids showed little to no detectable UCP1 signal and weaker PLIN1 staining (Fig. **8A**). This pattern was supported by quantification across all available patients and replicates (Fig. **8B**).

In all patient samples, DIFF BA spheroids exhibited higher UCP1 positivity than UND BA spheroids. In patient 117S, the mean UCP1-positive area fraction was 13.6% in BA DIFF spheroids and **0.0%** in BA UND spheroids. In patient 123S, the corresponding values were **41.9%** and **0.0%,** and in patient 124S they were **28.0%** and **0.03%,** respectively. Overall, the mean UCP1-positive area fraction across all three patients was **27.8%** in BA DIFF spheroids, compared with an almost absent signal in BA UND spheroids. Thus, differentiation was consistently associated with increased UCP1 staining in every patient analyzed.

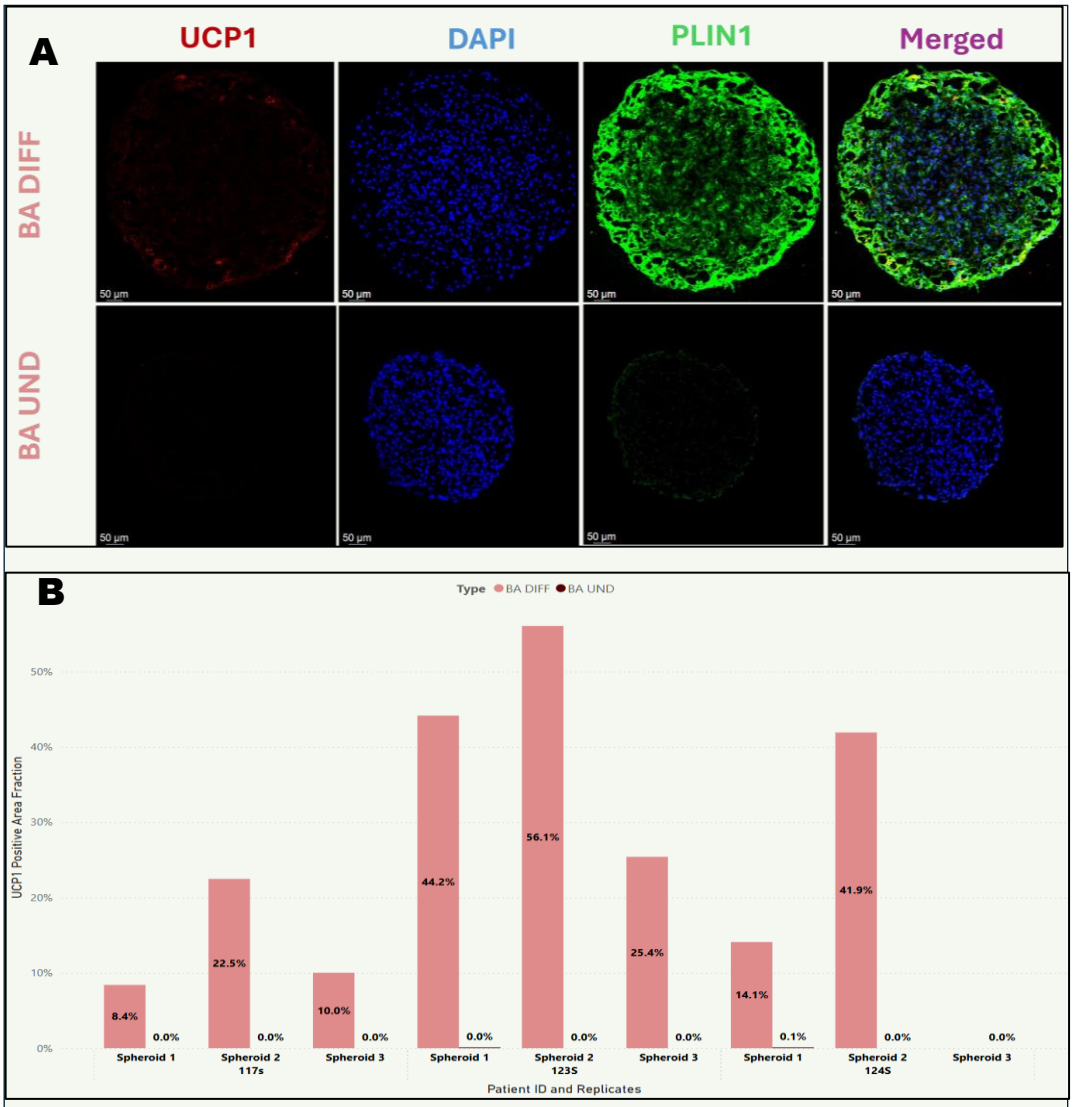

Figure 8.UCP1 expression in differentiated and undifferentiated brown adipose spheroids. ***(A)*** *Representative immunofluorescence images of BA spheroids from patient 117S stained for UCP1 (red), DAPI (blue), and PLIN1 (green). BA DIFF spheroids showed detectable UCP1 and stronger PLIN1 staining, whereas BA UND showed little to no UCP1 signal. Images were acquired at 20× magnification. Scale bars are shown in the panels.*
(B) *Quantification of UCP1-positive area fraction (%) in DIFF and UND BA spheroids from three patients (117S, 123S, and 124S), with individual spheroid replicates shown separately. differentiated spheroids showed clear UCP1 positivity across all patients, ranging from 8.4–22.5% in patient 117S, 25.4–56.1% in patient 123S, and 14.1–41.9% in patient 124S, whereas UND spheroids showed 0.0–0.1% positivity. Patient 124S spheroid 3 was available only in UND conditions and had no matching DIFF pair. The graph is consistent with panel A, showing that UCP1 expression is present in DIFF spheroids but absent or minimal in UND spheroids.*

A higher-magnification representative image from patient 123S further demonstrated PLIN1 staining together with detectable UCP1 signal in DIFF brown adipose spheroids (**Fig.9A**). Similarly, TEM images were consistent with these findings, as

BA DIFF displayed a more adipocyte-like morphology with visible lipid droplets and mitochondria, whereas BA UND retained a more undeveloped, organelle-rich appearance with less evident lipid accumulation (Fig. **9B**).

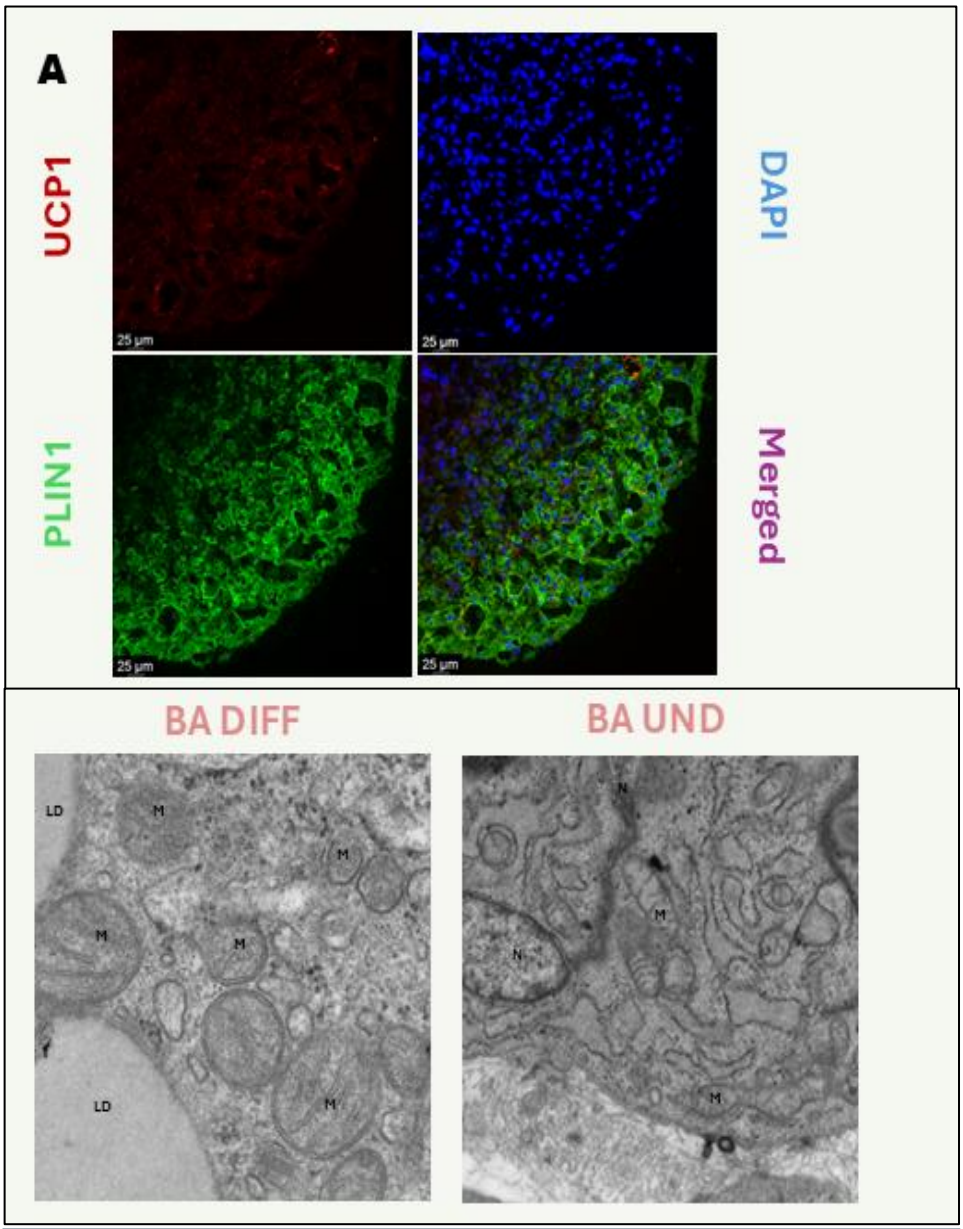

Figure 9. Immunofluorescence and ultrastructural comparison of DIFF and UND BA spheroids.
(A) Higher-magnification immunofluorescence image of a DIFF BA spheroid from patient 123S stained for UCP1, PLIN1, and DAPI. Images were acquired at 20× magnification; scale bars are shown in the panels. (B) Representative TEM images of DIFF and UND BA spheroids from patient 117S. DIFF spheroids show a more adipocyte-like ultrastructure with lipid droplets (LD) and mitochondria (M), whereas these features are minimal in UND spheroids. Overall, the ultrastructural findings support the immunofluorescence and quantitative data showing differentiation-associated BAT-like maturation.

In contrast, DIFF (WA) spheroids showed only minimal UCP1 positivity, with a mean UCP1-positive area fraction of **2.3%** across all patients. At the patient level, WA DIFF spheroids showed **0.0%** UCP1 positivity in patient 117S, **6.8%** in patient 123S, and **0.0%** in patient 124S. Representative images from patient 124S showed clear UCP1 staining in BA DIFF spheroids, whereas WA DIFF spheroids showed minimal signal (**Fig. 10A**). Quantification confirmed higher UCP1 positivity in BA DIFF than in WA DIFF in all patients examined (**Fig. 10B**). This comparison further supported the brown adipose-like phenotype of DIFF BA spheroids.

Patient 124S spheroid 3 was available only in UND conditions, because the matched DIFF spheroid did not meet the predefined quality criteria. Therefore, no matched DIFF value was available for this replicate.

Taken together, these results show that differentiation induced clear UCP1 expression predominantly in BA spheroids. Although the absolute UCP1-positive area fraction in DIFF BA spheroids was moderate (the values were obtained from unstimulated spheroids), it was clearly separated from the almost absent signal observed in BA UND spheroids and from the minimal signal detected in WA DIFF spheroids.

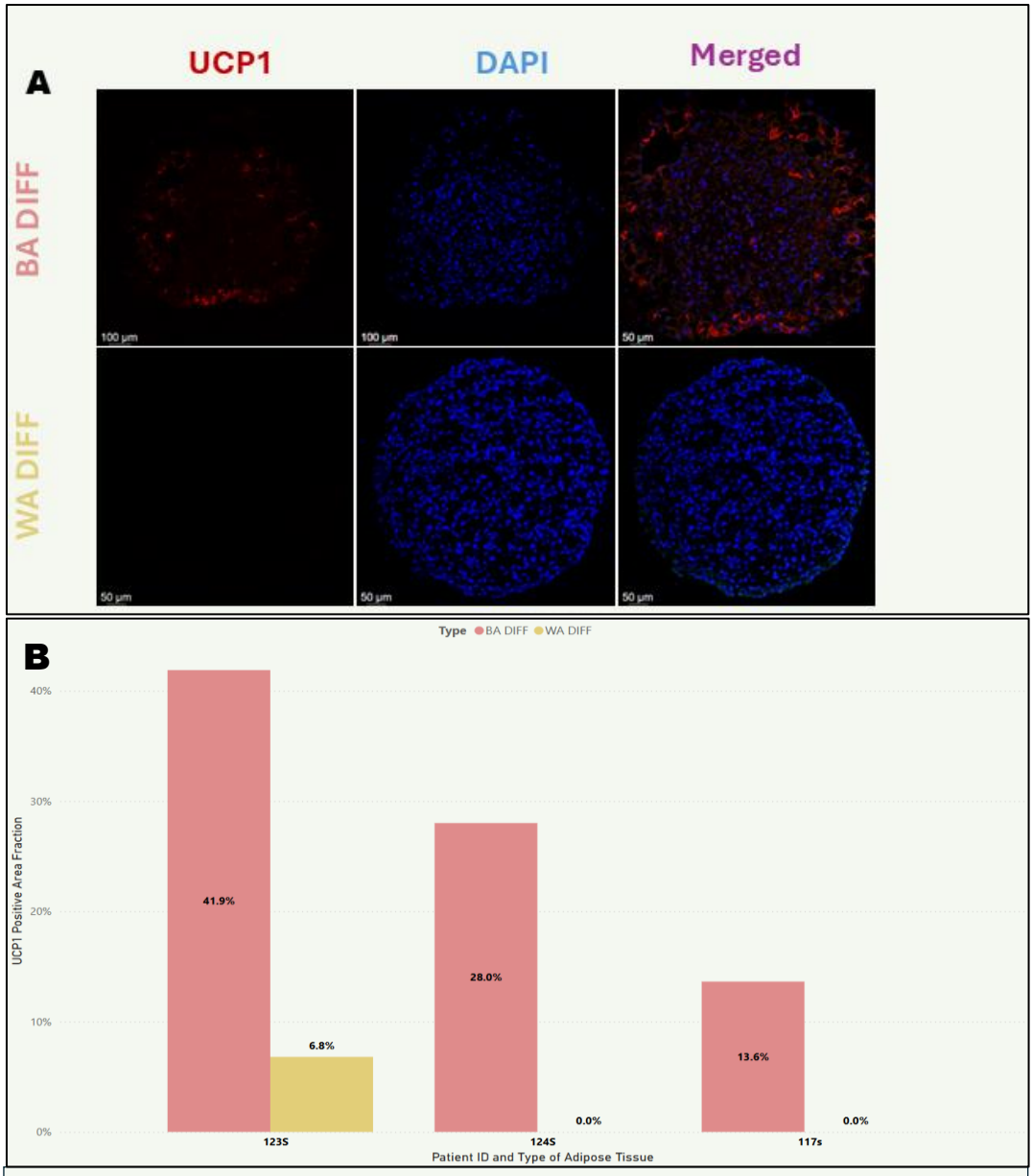

Figure 10. Brown adipose spheroids show higher UCP1 expression than white adipose spheroids after differentiation.

(A) *Representative immunofluorescence images from patient 124 of DIFF brown adipose (BA DIFF) and white adipose (WA DIFF) spheroids stained for UCP1 (red) and DAPI (blue), with merged images shown in the right column. UCP1 signal was clearly detected in BA DIFF spheroids, whereas WA DIFF spheroids showed little to no UCP1 staining. Images were acquired at 20× magnification. Scale bars are shown in the panels.* ***(B)*** *Quantification of mean UCP1-positive area fraction (%) in DIFF brown and white adipose spheroids from patients 123S, 1245, and 117S. BA DIFF spheroids showed higher UCP1 positivity than WA DIFF spheroids in all cases, with values of 41.9% vs 6.8% for patient 123S, 28.0% vs 0.0% for patient 1245, and 13.6% vs 0.0% for patient 117S. Thus, DIFF brown adipose spheroids consistently showed greater UCP1 expression than DIFF white adipose spheroids. A low UCP1-positive area fraction was detected in one WA DIFF spheroid from patient 123S (6.8%), representing a minor deviation from the otherwise absent WA UCP1 signal.*

.

4.2. CD31 Marker

CD31 positivity was detected in all spheroid groups, although the overall positive area remained low, with all values below **10%** (**Fig.11**). DIFF BA spheroids showed consistently higher CD31-positive area fractions than DIFF WA spheroids in all patients. In patient 117S, CD31 positivity was **6.6%** in BA DIFF and 1.3% in WA DIFF; in patient 123S, the corresponding values were 3.8% and 2.0%; and in patient 124S, they were **4.3%** and **1.6%,** respectively (**Fig.11**). Overall, the mean CD31-positive area fraction across all patients was **4.9%** in BA DIFF compared with **1.6%** in WA DIFF. Lower CD31 signal in WA DIFF spheroids may also reflect the reduced structural stability observed in this group by day 14.

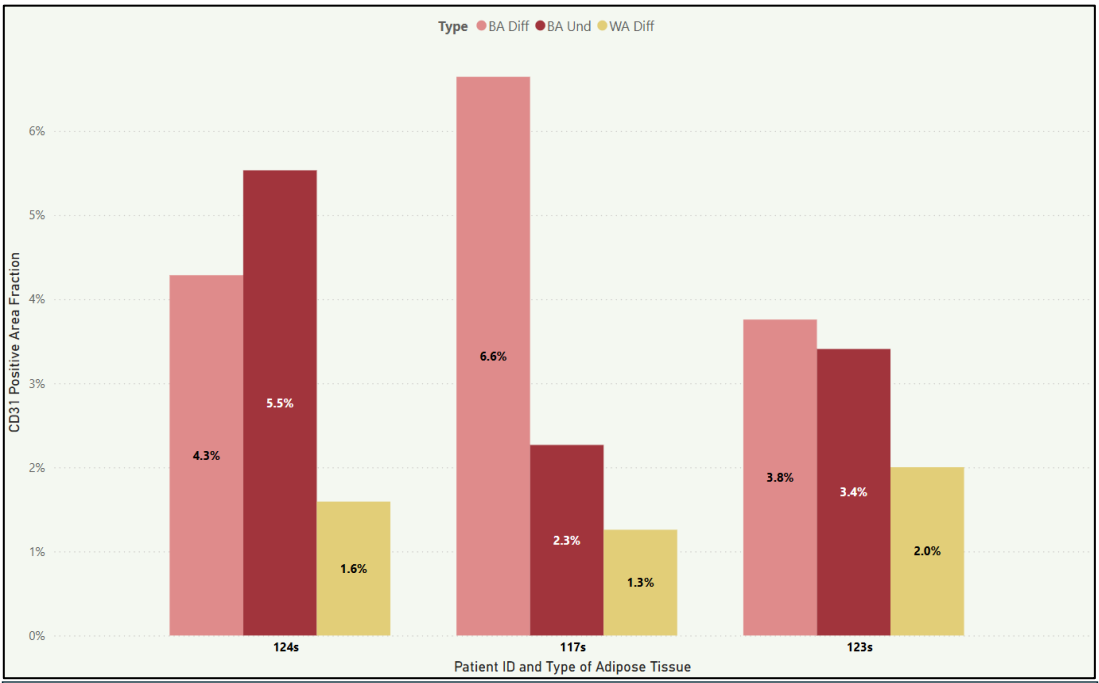

Figure 11.Quantification of CD31-positive area fraction in brown and white adipose spheroids. *CD31-positive area fraction (%) was measured in DIFF brown adipose spheroids (BA DIFF), UND brown adipose spheroids (BA Und), and DIFF white adipose spheroids (WA DIFF) from patients 124S, 117S, and 123S. CD31 positivity was detected in all spheroid groups, but the overall signal remained low, with all values below 10%. Among the three groups, BA DIFF generally showed the highest CD31-positive area fraction, with values of 4.3% (124S), 6.6% (117S), and 3.8% (123S). BA Und showed 5.5%, 2.3%, and 3.4%, respectively, while WA DIFF showed the lowest values overall, 1.6%, 1.3%, and 2.0%. The only exception to the overall trend was patient 124S, in which BA Und (5.5%) was slightly higher than BA DIFF (4.3%). Overall, the graph shows that CD31 signal was better retained in DIFF brown adipose spheroids than in the other groups, while DIFF white adipose spheroids consistently displayed the weakest signal.*

When compared with BA UND spheroids, the pattern was less uniform. BA DIFF showed higher CD31 positivity than BA UND in patients 117S and 123S, whereas in

patient 124S the BA UND spheroid showed a slightly higher value than the DIFF counterpart. The mean CD31-positive area fraction across all patients was **3.7%** in BA UND, compared with **4.9%** in BA DIFF. Thus, although CD31 signal remained low in all groups, DIFF BA spheroids tended to show higher CD31 positivity overall than BA UND and WA DIFF spheroids.

4.3. Cell Viability by Propidium Iodide (PI)

Overall, both BA and WA differentiated spheroids remained viable during culture. However, BA spheroids consistently showed higher average viability than WA spheroids in all three patients. This suggests that the culture conditions supported the maintenance of differentiated BA spheroids particularly well, while WA spheroids showed more variable and generally lower viability. The patient-by-patient viability results are shown in **Figure 12.**

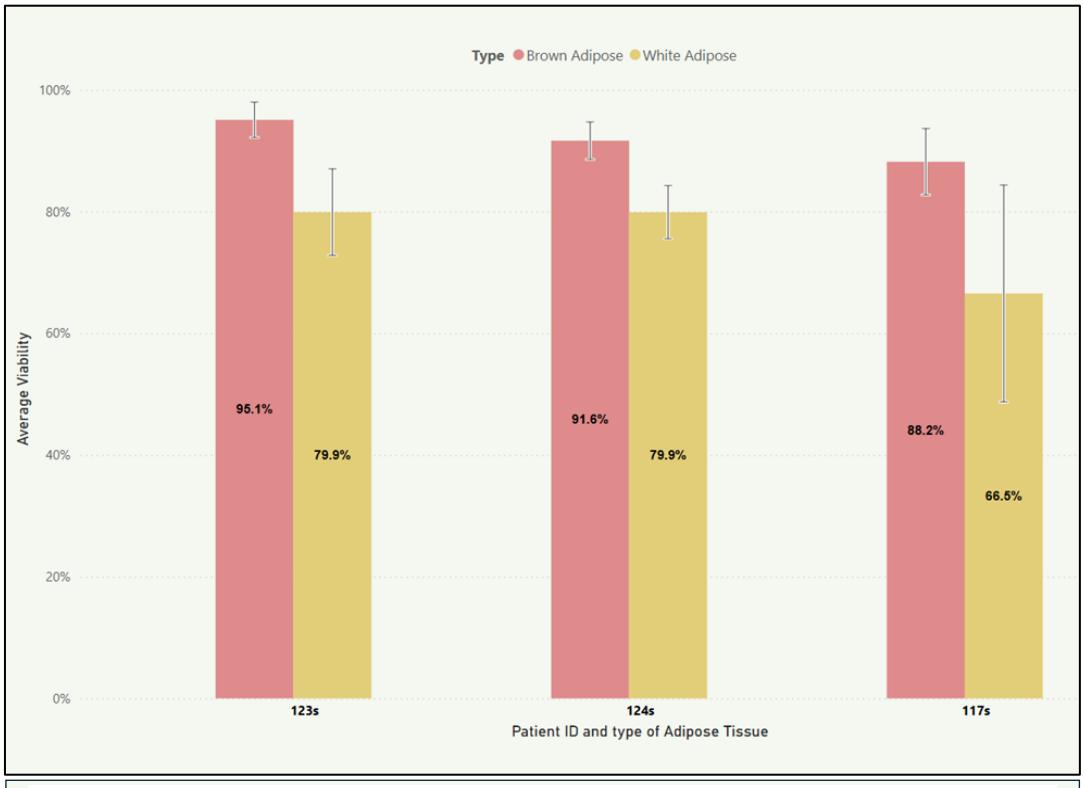

Figure 12. Average viability of differentiated brown adipose (BA) and white adipose (WA) spheroids from three patients, assessed by propidium iodide-based viability analysis. *BA spheroids showed consistently higher viability than WA spheroids across all donors. Error bars indicate standard deviation of biological replicates.*

Viability analysis showed that both DIFF BA and WA spheroids were substantially more viable than their corresponding ethanol-treated controls (**Fig. 13**). In BA DIFF spheroids, mean viability was **95.1%** in patient 123S, **91.6%** in patient 124S, and **88.2%** in patient 117S, whereas the corresponding control viabilities were **13.9%**, **7.1%,** and **7.6%**, respectively (**Fig. 13A**). In WA DIFF spheroids, mean viability was **79.9%** in patients 123S and 124S, and **66.5%** in patient 117S, while the corresponding control viabilities were **23.6%**, **13.4%**, and **27.7%**, respectively (**Fig. 13B)**

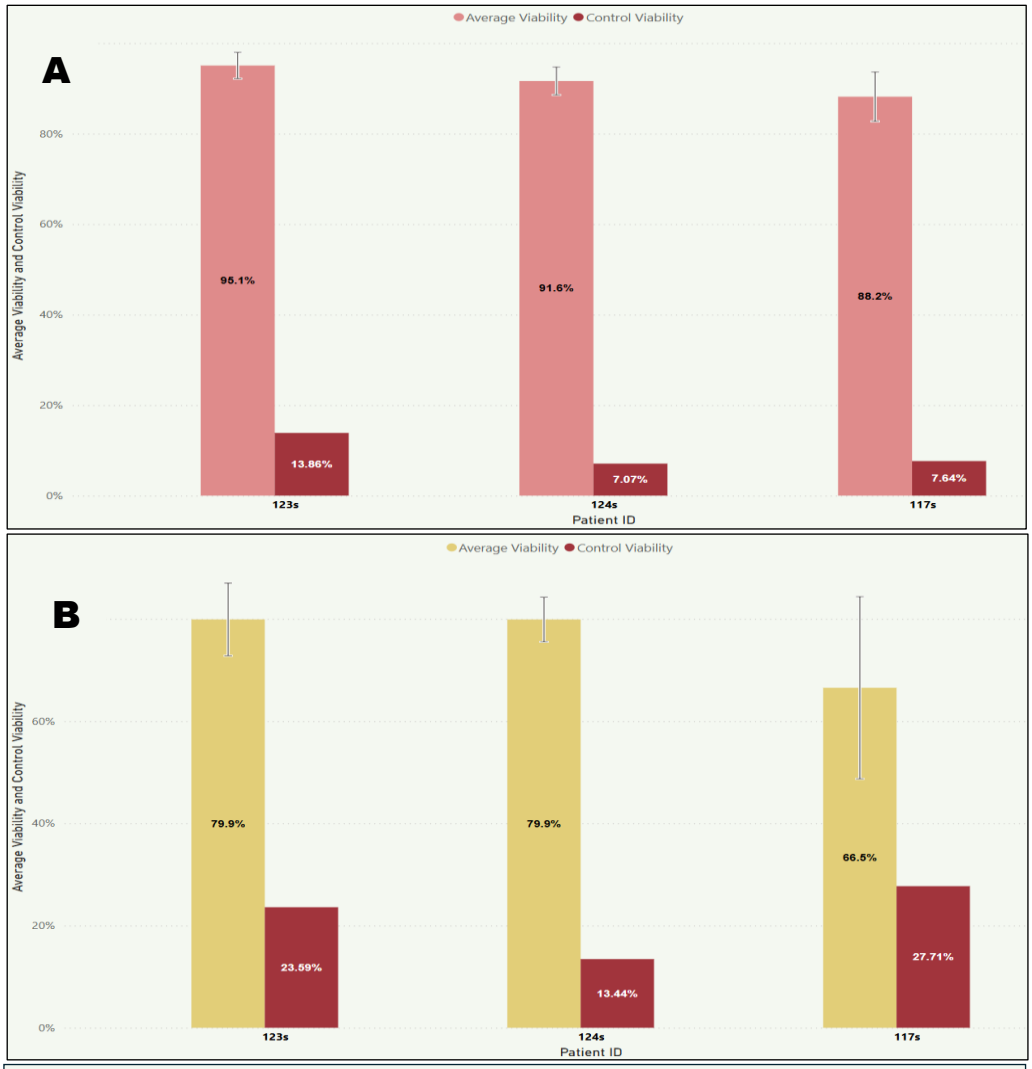

Figure 13.Quantification of spheroid viability shown separately for BA DIFF and WA DIFF spheroids together with their corresponding ethanol-treated controls.
(A) *In BA DIFF spheroids, average viability was 95.1% for patient 123S, 91.6% for 124S, and 88.2% for 117S, whereas the corresponding control values were 13.86%, 7.07%, and 7.64%, respectively.****(B)*** *In WA DIFF spheroids, average viability was 79.9% for patient 123S, 79.9% for 124S, and 66.6% for 117S, while the corresponding control values were 23.59%, 13.44%, and 27.71%, respectively. Overall, both DIFF spheroid types remained more viable than their ethanol-treated controls, although BA DIFF showed higher viability than WA DIFF across all patients*

To further examine this difference, viability was also assessed at the individual spheroid level. This showed the same trend, with most BA spheroids maintaining high viability, while WA spheroids showed greater variation between replicates. These spheroid-level results are shown in **Figure 14.**

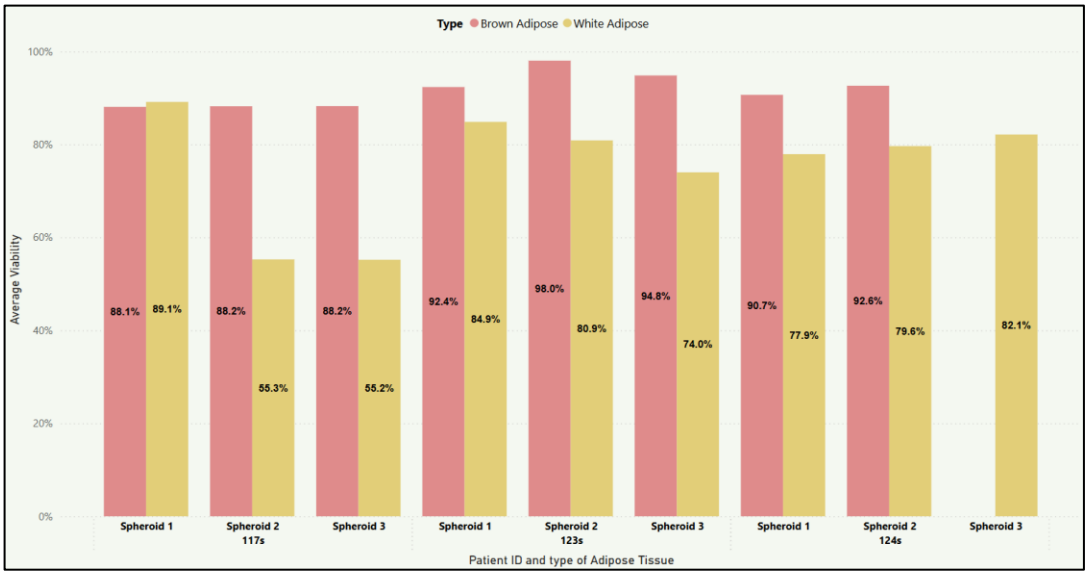

Figure 14. Spheroid-level viability of differentiated brown adipose (BA) and white adipose (WA) spheroids from three donors.
Each bar corresponds to one individual spheroid. BA has higher viability than WA across all replicates. This pattern further supports the conclusion that BA spheroids were more robustly maintained than WA spheroids under the present 3D culture conditions.

Representative images from patient 124S shown in **Figure 15** support the viability results. In both BA DIFF and WA DIFF spheroids, PI staining was limited, indicating that most cells remained viable. In contrast, the ethanol-treated controls showed strong PI signal throughout the spheroids because ethanol damages cell membranes and was used here as a non-viable control. This confirms that PI staining could clearly distinguish viable spheroids from non-viable controls.

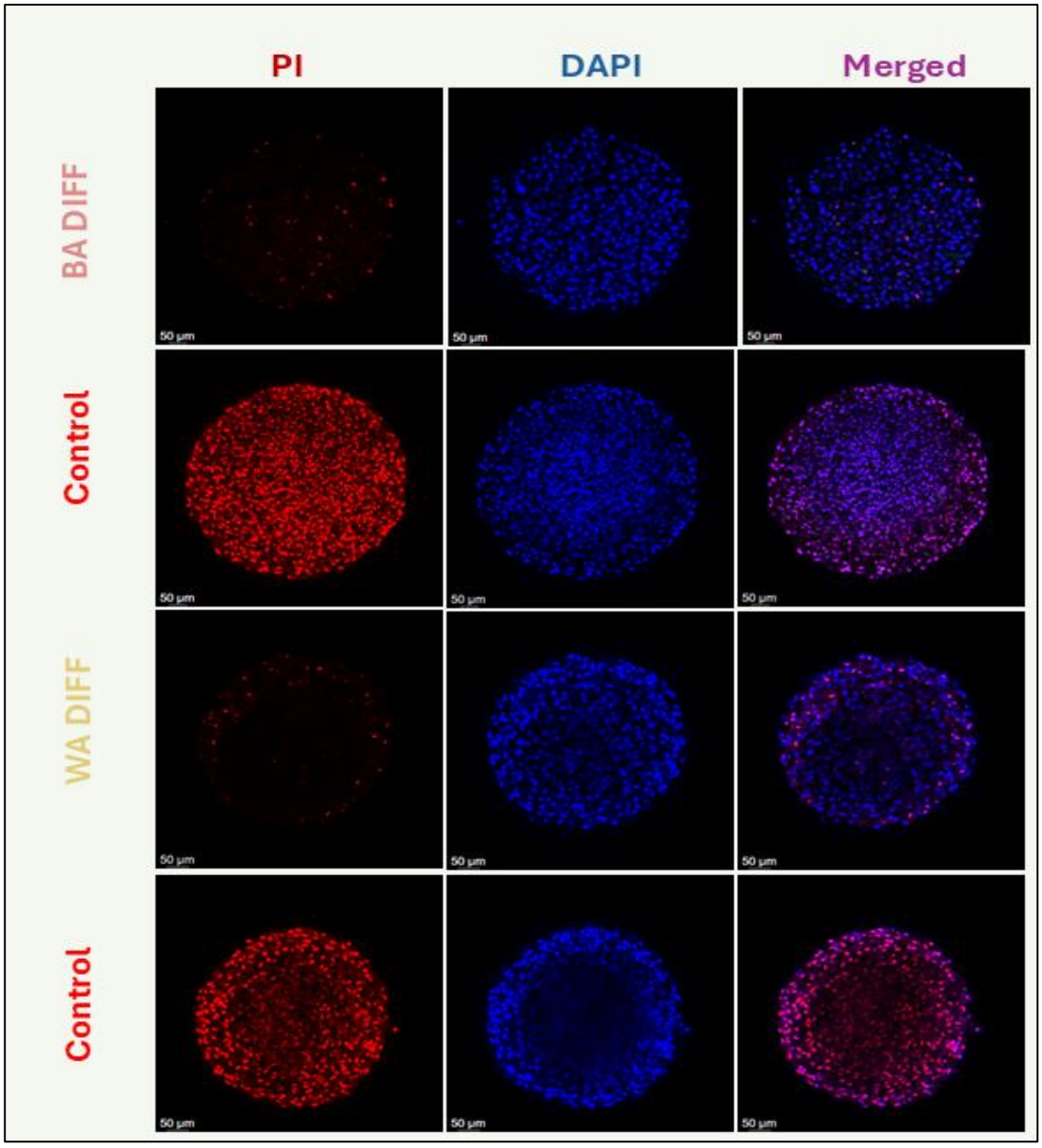

Figure 15. Representative images from patient 124S stained with propidium iodide.
Representative viability images of BA DIFF and WA DIFF spheroids from patient 124S, stained with propidium iodide (PI) (red) and DAPI (blue), with merged images shown in the right column. For each spheroid type, ethanol-treated control is shown to represent a non-viable condition. In the DIFF spheroids, PI signal was limited, indicating predominantly viable cells, whereas the ethanol-treated controls showed strong PI staining throughout the spheroid, consistent with extensive loss of viability. Scale bars are shown in the panels.

Calcein staining was used to visually check live cells in the spheroids. Calcein-AM gives green fluorescence in living, active cells, and in our samples this signal was clearly seen. Therefore, it supported that the spheroids contained viable cells. However, calcein was used only for visual confirmation, while the viability quantification was based on PI staining. Representative calcein staining is shown in **Figure 16.**

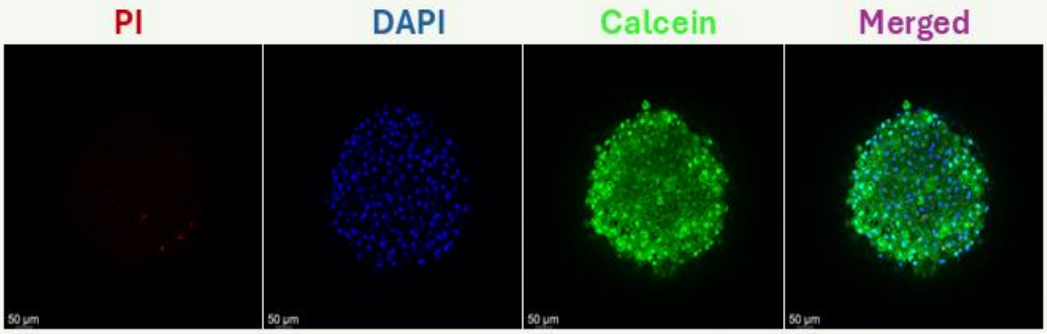

Figure 16. Representative fluorescence images of a differentiated spheroid from patient 123S stained with PI (red), DAPI (blue), and calcein (green).
Calcein labels metabolically active live cells, whereas PI marks cells with compromised plasma membranes. The merged image demonstrates predominant calcein staining and limited PI positivity. PI and calcein were used together for visualization, while viability quantification was based on PI staining only. Scale bars: 50 µm.

4.4. TEM

TEM analysis demonstrated clear ultrastructural differences between UND and DIFF BA spheroids **(Fig. 17).** In **BA UND**, cells showed expected morphology with organelle-rich cytoplasm with relatively large nuclei, prominent membranous cisternae consistent with the endomembrane system, and lysosome-like structures, while lipid accumulation remained limited **(Fig. 17 A-C).** In contrast, **BA DIFF** displayed hallmark features of BAT like large lipid droplets occupying most of the cell volume and mitochondria localized within the thin rim of remaining cytoplasm **(Fig. 17 D-F).** This clearly supports the idea that differentiation is associated with a clear shift from a dense, membrane-rich appearance to a lipid-filled mature adipocyte-like phenotype. In addition, a high-magnification image from patient 117S showed glycogen deposits **(Fig. 17 G)** which indicate active metabolism.

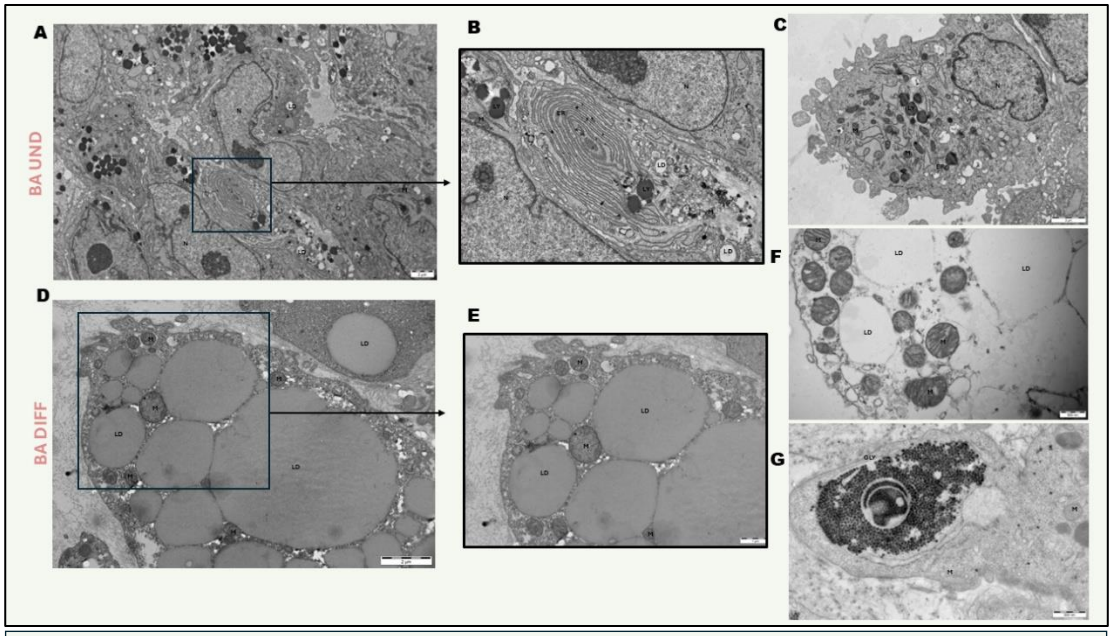

Figure 17. Transmission electron microscopy reveals clear ultrastructural differences between undifferentiated (UND) and differentiated (DIFF) BA spheroids. *(**A**) Representative TEM image of BA UND spheroid from patient 130s at 2500× magnification. **(B)** Higher-magnification view (5000×) of the boxed region in panel A, highlighting prominent stacked membranous cisternae and organelle-rich cytoplasm. **(C)** Additional TEM image of BA UND from the same patient at 3000× magnification. **(D**) Representative TEM image of BA DIFF spheroid from patient 130s at 3000× magnification. **(E)** Higher-magnification view (5000×) of the boxed region in panel D, showing large lipid droplets and mitochondria within the compressed cytoplasmic rim. **(F)** Additional high-magnification image of BA DIFF from the same patient at 8000× magnification. **(G)** High-magnification TEM image from patient 117S at 10000× magnification showing glycogen.*

Overall, BA UND cells displayed an immature ultrastructural appearance characterized by large nuclei, abundant endomembrane structures, lysosome-like compartments, and limited lipid accumulation, whereas BA DIFF cells showed a more adipocyte-like morphology with prominent lipid droplets and mitochondria distributed within the thin peripheral cytoplasm. Boxed areas indicate regions shown at higher magnification in the adjacent panels.

***Labels: N,** nucleus; **M**, mitochondrion; **LD**, lipid droplet; **ER**, endoplasmic reticulum; **LY**, lysosome-like structure; **GLY**, glycogen. Scale bars are shown in the panels.*

5. Discussion

Taken together, these findings indicate that the spheroid model was able to support BA like maturation at both the phenotypic and morphological level. The overall pattern was most clearly reflected by UCP1, which remained highest in DIFF BA spheroids and therefore supports the development of a thermogenic identity. In contrast, CD31 positivity remained low across groups, suggesting that endothelial features were limited in this model and were not a dominant component of the observed phenotype. At the same time, the viability results show that the culture conditions were able to maintain spheroid survival throughout the experiment, which is important for the usefulness of the model *in vitro* research. Furthermore, TEM findings also supported this interpretation by showing that differentiation was accompanied by clear ultrastructural changes that are consistent with adipocyte maturation and BAT phenotype acquisition.

5.1. UCP1 Marker

UCP1 is a canonical marker of BAT and one of the most important indicators of thermogenic identity, as it mediates mitochondrial uncoupling and non-shivering thermogenesis (*Bonet et al., 2017; Quan et al., 2024*). For this reason, assessing UCP1 levels is highly relevant when evaluating whether the adipose model truly exhibits BAT biology or is only showing general adipogenic differentiation. Simply put, while lipid accumulation and adipocyte-like morphology indicate maturation toward an adipose phenotype, UCP1 provides more specific evidence of thermogenic specialization, which is the defining functional feature of BA.

In the present study, DIFF BA spheroids showed clearly higher UCP1 positivity than the UND ones, indicating successful acquisition of a BA phenotype upon differentiation. This difference is biologically meaningful although UCP1 expression was moderate rather than extremely high. Importantly, the measurements were obtained under unstimulated basal conditions, without external thermogenic activation. This should be considered when interpreting the magnitude of the signal, as UCP1 expression is dynamic and strongly influenced by physiological and experimental stimuli. BA are known to express UCP1 even without external stimulation, whereas beige-like adipocytes within WAT generally require stimuli such as cold exposure or adrenergic activation to induce

detectable UCP1 expression (*Nedergaard and Cannon, 2014; Gong et al., 2024*). This likely explains the higher UCP1 levels observed in BA spheroids and the minimal signal detected in DIFF WA spheroids.

The donor-to-donor variation observed in UCP1-positive area fraction is also biologically expected and does not weaken the overall interpretation. Human adipose samples are inherently heterogeneous, and the thermogenic capacity of BA can vary between individuals (*Shinoda et al., 2015; Xue et al., 2015*) depending on factors such as cellular composition, differentiation efficiency, and intrinsic metabolic state. It should also be noted that the analysis was based on one section per spheroid and therefore may not fully represent UCP1 expression across the whole spheroid. Since UCP1 levels can vary between different regions of the same spheroid, the measured area fraction should be interpreted as a representative section-based estimate rather than a complete measure of the entire spheroid. Despite this limitation, the overall pattern remained highly consistent across the dataset: DIFF BA spheroids showed higher UCP1 positivity than UND BA spheroids in every patient, and exceeded the levels observed in DIFF WA spheroids. This consistency across all donors strengthens the conclusion that the observed signal reflects a genuine thermogenic phenotype rather than some random signal.

Although direct numerical comparison with previous studies is difficult, because UCP1 has been quantified using different methods across literature, the present findings are in clear agreement with earlier reports showing that brown adipose differentiation in 3D culture is associated with increased UCP1 expression. For example, *Wang et al., 2023* reported enhanced UCP1 expression in engineered human BA microtissues while *Klingelhutz et al., 2018* found significantly higher UCP1 expression in mouse BAT-derived spheroids than in corresponding 2D cell cultures. Thus, even though the readout used here was positive area fraction rather than gene expression or bulk protein quantification, the biological direction of the result is in line with previous work. This supports the interpretation that the present spheroid system captures an essential aspect of BA maturation in a 3D setting.

The immunofluorescence findings were also supported by the structural observations obtained from PLIN1 staining and transmission electron microscopy. DIFF BA spheroids showed stronger PLIN1 staining which visually confirms the presence of numerous small

lipid droplets. PLIN1 is a protein that coats lipid droplets. The TEM further revealed features more consistent with adipocyte maturation, including visible lipid droplets and abundant mitochondria. These observations are important because they place the UCP1 result into a broader biological context. Rather than relying on a single marker alone, the model showed converging evidence of BA differentiation at both the protein and ultrastructural level.

Although the present thesis assessed UCP1 expression mainly by immunofluorescence, additional experiments like qPCR and lipolysis assays were also conducted by other lab members as part of the broader project and UCP1 expression was also confirmed there.

Overall, the UCP1 results support that just like BA biology, our BA spheroids express the thermogenic hallmark marker UCP1 at the protein level under basal conditions. This further strengthens the hypothesis that the established spheroid model preserves the biologically relevant BA characteristics.

5.2. CD31 Marker

Low but detectable CD31 positivity was not an expected finding in the present spheroid model, because the culture conditions were designed primarily to support adipogenic spheroid differentiation rather than endothelial induction or maintenance. In adipose-derived models, more apparent endothelial differentiation is usually reported only when specific endothelial-supportive conditions are applied. For example, *Fischer et al., (2009)* showed that UND adipose-derived stem cells did not display endothelial characteristics unless they were supplemented with endothelial cell growth factors together with shear stress. In a more directly comparable study, *Escudero et al., 2023 and Muller et al., 2019* preserved endothelial cells using **Endothelial Cell Growth Medium (EGM2),** which then resulted in dense CD31-positive vascular networks and lumen-containing structures that remained visible during differentiation. Taken together, the literature suggests that robust vasculature in adipose-derived 3D systems usually depends on medium and factors that support endothelial generation or use of scaffolds like Matrigel *(Muller et al., 2019; Davidsen et al., 2024)* which were absent in the present study.

The low CD31 signal observed in the spheroids may therefore be explained by a minor CD31-positive population already present in the starting material. AT derived SVFs are

heterogeneous, and CD31-positive subpopulations have been described in these cells (*Dhumale et al., 2023*). Moreover, CD31 alone is not enough to confirm endothelial structure formation, since it is also expressed by several non-endothelial blood-derived cell types including platelets, monocytes, neutrophils, and some lymphocyte populations (*Lertkiatmongkol et al., 2016*). Therefore, the signal detected here most likely reflects persistence of a small residual CD31-positive cell population rather than clear evidence of mature endothelial organization.

5.3. Viability

Assessment of viability is an important step when establishing a 3D spheroid model, because such models are intended to support extensive analysis and are increasingly used for translational applications such as drug screening and personalized *in vitro* testing. Thus, viability is not merely a technical readout, but an essential indicator that the model represents functional tissue rather than a structurally intact but biologically compromised aggregate. In this context, the high viability observed in DIFF BA spheroids is an important finding, because it indicates that the spheroids remained biologically intact under the applied culture conditions and were suitable for further structural and marker-based characterization.

DIFF WA spheroids showed lower viability, and this was also observed as a visible loss of structural stability in the WA group from day 14 onward. The most careful interpretation is that the culture conditions were less supportive for long-term maintenance of WA spheroids than for BA spheroids. This is supported by the study conducted by *Rogal et al., (2020)*, which noted that mature white adipocytes are particularly difficult to maintain long-term *in vitro* because of their buoyancy, fragility, and tendency to dedifferentiate. These features may help explain why WA spheroids appeared less stable and less viable in the present study. However, as these underlying mechanisms were not directly measured here, they should be considered contextual support rather than direct conclusions from the PI-based assay itself.

PI is a well-established marker for membrane-compromised cells and has been widely used in viability assessment in 3D culture studies, including adipose and spheroid-based models. In many studies, PI is used to visualize dead cell populations (for example by *Escudero et al., 2023; Schafer et al., 2013; Schopow et al., 2020; Wolff et al., 2022; Yu*

et al., 2024). Calcein labels metabolically active live cells whereas PI labels cells with compromised plasma membranes.

In our current study, both stains were combined for visualization purposes, as shown in **Figure 16**, but the quantitative analysis was based only on PI staining. This approach provided a clear and practical estimate of cell death within the spheroids, while the combined staining offered additional visual confirmation of overall viability.

Overall, the viability results strengthen the relevance of the BA spheroid model by showing that it maintained a high proportion of viable cells under the applied culture conditions. This is an important outcome for the thesis, because it supports that the other marker measurements were obtained from living and structurally preserved spheroids rather than from deteriorating cell aggregates. The spheroid-level data shown in **Figure 14** further supports this interpretation by demonstrating that the same trend was already visible at the level of individual spheroids.

Taken together, these findings support that the BA spheroid model remained both structurally intact and biologically viable, which is essential for reliable downstream characterization and future translational use.

5.4. TEM

TEM was used to complement and validate immunofluorescence imaging findings and to provide deeper insight into the ultrastructure of the spheroids. In the UND spheroids, cytoplasm appeared relatively rich in organelles and the nuclei were generally larger, while lipid accumulation and mitochondrial abundance remained low. After differentiation, their appearance changed clearly. The cells contained multiple large lipid droplets occupying most of the intracellular space, whereas the remaining cytoplasm formed a thin rim enriched with numerous mitochondria. These observations are important because they reflect key structural characteristics of BA which are closely linked to their thermogenic function (*Herbers et al., 2022; Cui et al., 2019*).

The identification of these ultrastructural features was also technically meaningful, since adipose samples are known to be challenging to prepare for TEM. Lipid morphology is hard to preserve along with other organelles and also prone to damage or loss during processing. For this reason, careful optimization of the fixation protocol was essential,

and the final protocol provided the best preservation of lipid droplets, mitochondria, and other intracellular structures altogether. Similar challenges and the need for optimized fixation have also been described in earlier studies of brown adipose tissue ultrastructure (*Chun-Chun et al., 2023*).

Overall, these findings show that differentiation not only changed expression of the measured markers but also gave rise to morphological features that are typical of BA. This is an important point, because it indicates that the observed phenotype was supported not only at the fluorescence level, but also at the ultrastructural level. Thus, TEM provided independent ultrastructural support that differentiation promoted the acquisition of a BA like phenotype in the spheroids.

5.5. Limitations and future implications

While this study successfully established and characterized a human BA spheroid model, some limitations also highlight important directions for future work. Lipid droplet morphology was assessed qualitatively rather than quantitatively, and parameters such as droplet size, area, and distribution were not measured systematically, even though these would have provided additional structural detail and were part of the original plan.

For CD31, future optimization could include the addition of pro-angiogenic or endothelial-supporting factors to improve the maintenance of CD31-positive cells within the spheroids. Ultrastructural analysis was also limited in scope, as only BA UND and BA DIFF spheroids could be examined by TEM. This was partly because optimization of fixation and processing required considerable time, and partly because periods of technical downtime in both the TEM and confocal microscope further restricted the planned analyses.

Nevertheless, the study provides consistent phenotypic, morphological and viability-based evidence that the model captures key features of BA after differentiation. Additionally, the image analysis pipelines were developed specifically for this work, providing a reproducible framework that can be further refined and expanded in future studies. The study not only establishes a human BA spheroid model but also provides a reproducible methodological foundation for its further development and application.

6. Conclusion

In conclusion, this study successfully established and characterized a human BA spheroid model that preserved key features of BAT after differentiation, including detectable UCP1 expression, lipid-rich adipocyte-like morphology, abundant mitochondria, and high viability. Together, these findings support the idea that the model is not only structurally formed, but also biologically relevant and sufficiently maintained for further phenotypic and functional studies.

Beyond the present results, models such as these are becoming increasingly important in biomedical research because they provide human-relevant 3D systems that can bridge the gap between simplified 2D cultures and *vivo* studies. Recent reviews describe adipose organoids and related 3D adipose models as promising platforms for studying AT development, metabolic disease mechanisms, and therapeutic responses, particularly because they can mimic structural and functional features of native tissue more closely than conventional *in vitro* systems (*Liu et al., 2024; Okumuş et al., 2024*).

At the same time, regulatory bodies such as the FDA are increasingly promoting human-relevant alternative methods that can reduce, refine, and potentially replace animal testing while improving translational predictivity

Thus, the present human BA spheroid model is relevant not only for BAT research, but also as part of a broader move toward more translatable and human-specific experimental platforms.

7. Acknowledgments

I would like to express my sincere gratitude to the BAT group for giving me the opportunity to carry out this thesis project and for providing a supportive and encouraging research environment.

I am grateful to **Kirsi Virtanen** for giving me the opportunity to work in the group and for her guidance and support during this thesis.

I would like to give my warmest thanks to **Johanna Örling** and **Francisco Acosta Manzano** for their continuous guidance, patience, and practical support throughout the project. Their teaching, feedback, and encouragement helped me understand the methods, interpret the results, and become more confident during the thesis process.

I am deeply thankful to my **parents** for their constant love, support, and motivation from far away. Their encouragement has always given me strength.

I would also like to thank my husband, **Danish**, for believing in me, supporting me, and motivating me throughout this journey. I am especially grateful to my little daughter, **Ayra**, whose love, joy, and presence gave me comfort and motivation during this process.

Finally, I would like to thank **Michal Skruzny** for proofreading my thesis and providing helpful comments.

I am sincerely thankful to everyone who supported me during this thesis journey.

References

Berry, D.C., Y. Jiang, R.W. Arpke, E.L. Close, A. Uchida, D. Reading, E.D. Berglund, M. Kyba, and J.M. Graff. 2017. Cellular Aging Contributes to Failure of Cold-Induced Beige Adipocyte Formation in Old Mice and Humans. *Cell Metab.* 25:481. doi:10.1016/j.cmet.2017.01.011.

Bonet, M.L., J. Mercader, and A. Palou. 2017. A nutritional perspective on UCP1-dependent thermogenesis. *Biochimie*. 134:99–117. doi:10.1016/j.biochi.2016.12.014.

Bredenoord, A.L., H. Clevers, and J.A. Knoblich. 2017. Human tissues in a dish: The research and ethical implications of organoid technology. *Science (1979).* 355:eaaf9414. doi:10.1126/science.aaf9414.

Chi, J., A. Crane, Z. Wu, and P. Cohen. 2018. Adipo-Clear: A Tissue Clearing Method for Three-Dimensional Imaging of Adipose Tissue. *JoVE*. e58271. doi:10.3791/58271.

Chun-Chun, W.E.I., W. Ping, L.I.N. Fang-Xing, M.A. Xian-Hua, Z. Wei-Ping, and X.I.E. Zhi-Fang. 2023. An improved fixation method for preparing mouse brown adipose tissue for transmission electron microscopy. *Acta Anatomica Sinica*. 54:738–743. doi:10.16098/j.issn.0529-1356.2023.06.017.

Cui, L., A.H. Mirza, S. Zhang, B. Liang, and P. Liu. 2019. Lipid droplets and mitochondria are anchored during brown adipocyte differentiation. *Protein Cell*. 10:921–926. doi:10.1007/s13238-019-00661-1.

Cypess, A.M., B. Cannon, J. Nedergaard, L. Kazak, D.C. Chang, J. Krakoff, Y.H. Tseng, C. Schéele, J. Boucher, N. Petrovic, D.P. Blondin, A.C. Carpentier, K.A. Virtanen, S. Kooijman, P.C.N. Rensen, C. Cero, and S. Kajimura. 2025. Emerging debates and resolutions in brown adipose tissue research. *Cell Metab.* 37:12–33. doi:10.1016/j.cmet.2024.11.002.

Cypess, A.M., S. Lehman, G. Williams, I. Tal, D. Rodman, A.B. Goldfine, F.C. Kuo, E.L. Palmer, Y.-H. Tseng, A. Doria, G.M. Kolodny, and C.R. Kahn. 2009. Identification and Importance of Brown Adipose Tissue in Adult Humans. *New England Journal of Medicine*. 360:1509–1517. doi:10.1056/NEJMoa0810780.

Davidsen, L.I., C.E. Hagberg, V. Goitea, S.M. Lundby, S. Larsen, M.F. Ebbesen, N. Stanic, H. Topel, and J.-W. Kornfeld. 2024. Mouse vascularized adipose spheroids: an organotypic model for thermogenic adipocytes. *Front. Endocrinol. (Lausanne).* Volume 15-2024. doi:10.3389/fendo.2024.1396965.

Dhumale, P., J.V. Nielsen, A.C.S. Hansen, M. Burton, H.C. Beck, M.G. Jørgensen, N.M. Toyserkani, M.K. Haahr, S.T. Hansen, L. Lund, M. Thomassen, J.A. Sørensen, D.C. Andersen, C.H. Jensen, and S.P. Sheikh. 2023. CD31 defines a subpopulation of human adipose-derived regenerative cells with potent angiogenic effects. *Sci. Rep.* 13:14401. doi:10.1038/s41598-023-41535-1.

Escudero, M., L. Vaysse, G. Eke, M. Peyrou, F. Villarroya, S. Bonnel, Y. Jeanson, L. Boyer, C. Vieu, B. Chaput, X. Yao, F. Deschaseaux, M. Parny, I. Raymond-Letron, C. Dani, A. Carrière, L. Malaquin, and L. Casteilla. 2023a. Scalable Generation of Pre-Vascularized and Functional Human Beige Adipose Organoids. *Advanced Science*. 10:2301499. doi:10.1002/advs.202301499.

Escudero, M., L. Vaysse, G. Eke, M. Peyrou, F. Villarroya, S. Bonnel, Y. Jeanson, L. Boyer, C. Vieu, B. Chaput, X. Yao, F. Deschaseaux, M. Parny, I. Raymond-Letron, C. Dani, A. Carrière, L. Malaquin, and L. Casteilla. 2023b. Scalable Generation of Pre-Vascularized and Functional Human Beige Adipose Organoids. *Advanced Science*. 10. doi:10.1002/advs.202301499.

Fedorenko, A., P.V. Lishko, and Y. Kirichok. 2012. Mechanism of Fatty-Acid-Dependent UCP1 Uncoupling in Brown Fat Mitochondria. *Cell*. 151:400–413. doi:10.1016/j.cell.2012.09.010.

Feldmann, H.M., V. Golozoubova, B. Cannon, and J. Nedergaard. 2009. UCP1 Ablation Induces Obesity and Abolishes Diet-Induced Thermogenesis in Mice Exempt from Thermal Stress by Living at Thermoneutrality. *Cell Metab.* 9:203–209. doi:10.1016/j.cmet.2008.12.014.

Fischer, L.J., S. McIlhenny, T. Tulenko, N. Golesorkhi, P. Zhang, R. Larson, J. Lombardi, I. Shapiro, and P.J. DiMuzio. 2009. Endothelial Differentiation of Adipose-Derived Stem Cells: Effects of Endothelial Cell Growth Supplement and Shear Force. *Journal of Surgical Research*. 152:157–166. doi:10.1016/j.jss.2008.06.029.

Gong, D., J. Lei, X. He, J. Hao, F. Zhang, X. Huang, W. Gu, X. Yang, and J. Yu. 2024. Keys to the switch of fat burning: stimuli that trigger the uncoupling protein 1 (UCP1) activation in adipose tissue. *Lipids Health Dis.* 23:322. doi:10.1186/s12944-024-02300-z.

de Gonzalez, A.B., P. Hartge, J.R. Cerhan, A.J. Flint, L. Hannan, R.J. MacInnis, S.C. Moore, G.S. Tobias, H. Anton-Culver, L.B. Freeman, W.L. Beeson, S.L. Clipp, D.R. English, A.R. Folsom, D.M. Freedman, G. Giles, N. Hakansson, K.D. Henderson, J. Hoffman-Bolton, J.A. Hoppin, K.L. Koenig, I.-M. Lee, M.S. Linet, Y. Park, G. Pocobelli, A. Schatzkin, H.D. Sesso, E. Weiderpass, B.J. Willcox, A. Wolk, A. Zeleniuch-Jacquotte, W.C. Willett, and M.J. Thun. 2010. Body-Mass Index and Mortality among 1.46 Million White Adults. *New England Journal of Medicine*. 363:2211–2219. doi:10.1056/NEJMoa1000367.

Gunti, S., A.T.K. Hoke, K.P. Vu, and N.R. London. 2021. Organoid and Spheroid Tumor Models: Techniques and Applications. *Cancers (Basel).* 13. doi:10.3390/cancers13040874.

Ha, M., T. Leng, J. Jiang, X. Ma, Y. Chen, T. Hu, Y. Huang, and C. Rao. 2026. Brown adipocytes from pluripotent stem cells: a promising therapy for obesity. *Mol. Biol. Rep.* 53. doi:10.1007/s11033-025-11281-w.

Harms, M., and P. Seale. 2013. Brown and beige fat: development, function and therapeutic potential. *Nat. Med.* 19:1252–1263. doi:10.1038/nm.3361.

Herbers, E., M. Patrikoski, A. Wagner, R. Jokinen, A. Hassinen, S. Heinonen, S. Miettinen, H. Peltoniemi, E. Pirinen, and K.H. Pietiläinen. 2022. Preventing White Adipocyte Browning during Differentiation in Vitro: The Effect of Differentiation Protocols on Metabolic and Mitochondrial Phenotypes. *Stem Cells Int.* 2022. doi:10.1155/2022/3308194.

Jacene, H.A., C.C. Cohade, Z. Zhang, and R.L. Wahl. 2011. The Relationship between Patients' Serum Glucose Levels and Metabolically Active Brown Adipose Tissue Detected by PET/CT. *Mol. Imaging Biol.* 13:1278–1283. doi:10.1007/s11307-010-0379-9.

Kajimura, S. 2025. An Unexpected Journey Into Brown Fat Research for Metabolic Health: The 2025 Outstanding Scientific Achievement Award Lecture. *Diabetes*. 74:2216–2222. doi:10.2337/dbi25-0026.

Klingelhutz, A.J., F.A. Gourronc, A. Chaly, D.A. Wadkins, A.J. Burand, K.R. Markan, S.O. Idiga, M. Wu, M.J. Potthoff, and J.A. Ankrum. 2018. Scaffold-free generation of uniform adipose spheroids for metabolism research and drug discovery. *Sci. Rep.* 8:523. doi:10.1038/s41598-017-19024-z.

Kobolak, J., A. Teglasi, T. Bellak, Z. Janstova, K. Molnar, M. Zana, I. Bock, L. Laszlo, and A. Dinnyes. 2020. Human Induced Pluripotent Stem Cell-Derived 3D-Neurospheres Are Suitable for Neurotoxicity Screening. *Cells*. 9. doi:10.3390/cells9051122.

Kraljević, M., J. Süsstrunk, B.K. Wölnerhanssen, T. Peters, M. Bueter, D. Gero, B. Schultes, A. Poljo, R. Schneider, and R. Peterli. 2025. Long-Term Outcomes of Laparoscopic Roux-en-Y Gastric Bypass vs Laparoscopic Sleeve Gastrectomy for Obesity: The SM-BOSS Randomized Clinical Trial. *JAMA Surg.* 160:369–377. doi:10.1001/jamasurg.2024.7052.

Lee, H.J., J. Lee, M.J. Yang, Y.-C. Kim, S.P. Hong, J.M. Kim, G.-S. Hwang, and G.Y. Koh. 2023. Endothelial cell-derived stem cell factor promotes lipid accumulation through c-Kit-mediated increase of lipogenic enzymes in brown adipocytes. *Nat. Commun.* 14:2754. doi:10.1038/s41467-023-38433-5.

Lee, P., J.R. Greenfield, K.K.Y. Ho, and M.J. Fulham. 2010. A critical appraisal of the prevalence and metabolic significance of brown adipose tissue in adult humans. *American Journal of Physiology-Endocrinology and Metabolism*. 299:E601–E606. doi:10.1152/ajpendo.00298.2010.

Lee, P., M.M. Swarbrick, J.T. Zhao, and K.K.Y. Ho. 2011. Inducible Brown Adipogenesis of Supraclavicular Fat in Adult Humans. *Endocrinology*. 152:3597–3602. doi:10.1210/en.2011-1349.

Lertkiatmongkol, P., D. Liao, H. Mei, Y. Hu, and P.J. Newman. 2016. Endothelial functions of platelet/endothelial cell adhesion molecule-1 (CD31). *Curr. Opin. Hematol.* 23. doi:10.1097/MOH.0000000000000239.

Liu, X., J. Yang, Y. Yan, Q. Li, and R.-L. Huang. 2024. Unleashing the potential of adipose organoids: A revolutionary approach to combat obesity-related metabolic diseases. *Theranostics*. 14:2075–2098. doi:10.7150/thno.93919.

Luo, T., L. Chen, K. Tu, L. Jiang, S. Liang, S. Wang, Y. Huang, and X. Yang. 2025. Adipose tissue-targeted drug delivery for treating obesity: current opportunities and challenges. *Drug Deliv.* 32. doi:10.1080/10717544.2025.2547751.

Mandl, M., H.P. Viertler, F.M. Hatzmann, C. Brucker, S. Großmann, P. Waldegger, T. Rauchenwald, M. Mattesich, M. Zwierzina, G. Pierer, and W. Zwerschke. 2022. An organoid model derived from human adipose stem/progenitor cells to study adipose tissue physiology. *Adipocyte*. 11:164–174. doi:10.1080/21623945.2022.2044601.

van Marken Lichtenbelt, W.D., J.W. Vanhommerig, N.M. Smulders, J.M.A.F.L. Drossaerts, G.J. Kemerink, N.D. Bouvy, P. Schrauwen, and G.J.J. Teule. 2009. Cold-Activated Brown Adipose Tissue in Healthy Men. *New England Journal of Medicine*. 360:1500–1508. doi:10.1056/NEJMoa0808718.

Martinez-Santibañez, G., K.W. Cho, and C.N. Lumeng. 2014. Chapter Two - Imaging White Adipose Tissue with Confocal Microscopy. *In* Methods in Enzymology. O.A. Macdougald, editor. Academic Press. 17–30.

Mihoko, Y., K.B. D, Y. Jun, S.R. I, R. Dominic, E.J. Christopher, E.S. R, W.J. D, J. Mohit, K. Rob, S. Kenneth, P.B. W, and K. Samuel. 2020. Effects of Diet versus Gastric Bypass on Metabolic Function in Diabetes. *New England Journal of Medicine*. 383:721–732. doi:10.1056/NEJMoa2003697.

Muller, S., I. Ader, J. Creff, H. Leménager, P. Achard, L. Casteilla, L. Sensebé, A. Carrière, and F. Deschaseaux. 2019. Human adipose stromal-vascular fraction self-organizes to form vascularized adipose tissue in 3D cultures. *Sci. Rep.* 9:7250. doi:10.1038/s41598-019-43624-6.

Nedergaard, J., and B. Cannon. 2014. The Browning of White Adipose Tissue: Some Burning Issues. *Cell Metab.* 20:396–407. doi:10.1016/j.cmet.2014.07.005.

Okumuş, E.B., Ö.B. Böke, S.Ş. Turhan, and A. Doğan. 2024. From development to future prospects: The adipose tissue & adipose tissue organoids. *Life Sci.* 351:122758. doi:10.1016/j.lfs.2024.122758.

Ouellet, V., A. Routhier-Labadie, W. Bellemare, L. Lakhal-Chaieb, E. Turcotte, A.C. Carpentier, and D. Richard. 2011. Outdoor Temperature, Age, Sex, Body Mass Index, and Diabetic Status Determine the Prevalence, Mass, and Glucose-Uptake Activity of 18F-FDG-Detected BAT in Humans. *J. Clin. Endocrinol. Metab.* 96:192–199. doi:10.1210/jc.2010-0989.

Pilkington, A.C., H.A. Paz, and U.D. Wankhade. 2021. Beige Adipose Tissue Identification and Marker Specificity—Overview. *Front. Endocrinol. (Lausanne).* 12. doi:10.3389/fendo.2021.599134.

Powis, J., R. Thompson, and R. Jackson-Leach. 2025. World Obesity Atlas 2025. London.

Prospective Studies Collaborations. 2009. Body-mass index and cause-specific mortality in 900 000 adults: collaborative analyses of 57 prospective studies. *The Lancet*. 373:1083–1096. doi:10.1016/S0140-6736(09)60318-4.

Quan, Y., F. Lu, and Y. Zhang. 2024. Use of brown adipose tissue transplantation and engineering as a thermogenic therapy in obesity and metabolic disease. *Obesity Reviews*. 25:e13677. doi:10.1111/obr.13677.

Robledo, F., L. González-Hodar, P. Tapia, A.-M. Figueroa, F. Ezquer, and V. Cortés. 2023. Spheroids derived from the stromal vascular fraction of adipose tissue self-organize in complex adipose organoids and secrete leptin. *Stem Cell Res. Ther.* 14:70. doi:10.1186/s13287-023-03262-2.

Rogal, J., C. Binder, E. Kromidas, J. Roosz, C. Probst, S. Schneider, K. Schenke-Layland, and P. Loskill. 2020. WAT-on-a-chip integrating human mature white adipocytes for mechanistic research and pharmaceutical applications. *Sci. Rep.* 10:6666. doi:10.1038/s41598-020-63710-4.

S, C.L.M., S. Kajsa, J. Peter, A.-A.J. C, S. Per-Arne, T. Magdalena, C. Björn, and P. Markku. 2020. Life Expectancy after Bariatric Surgery in the Swedish Obese Subjects Study. *New England Journal of Medicine*. 383:1535–1543. doi:10.1056/NEJMoa2002449.

Saito, M., Y. Okamatsu-Ogura, M. Matsushita, K. Watanabe, T. Yoneshiro, J. Nio-Kobayashi, T. Iwanaga, M. Miyagawa, T. Kameya, K. Nakada, Y. Kawai, and M. Tsujisaki. 2009. High incidence of metabolically active brown adipose tissue in healthy adult humans: effects of cold exposure and adiposity. *Diabetes*. 58:1526+.

Sakers, A., M.K. De Siqueira, P. Seale, and C.J. Villanueva. 2022. Adipose-tissue plasticity in health and disease. *Cell*. 185:419–446. doi:10.1016/j.cell.2021.12.016.

Schafer, M., K. Hicok, D. Mills, S. Cohen, and J. Chao. 2013. Acute Adipocyte Viability After Third-Generation Ultrasound-Assisted Liposuction. *Aesthetic surgery journal / the American Society for Aesthetic Plastic surgery*. 33. doi:10.1177/1090820X13485239.

Scheele, C., and C. Wolfrum. 2020. Brown Adipose Crosstalk in Tissue Plasticity and Human Metabolism. *Endocr. Rev.* 41:53–65. doi:10.1210/endrev/bnz007.

Scherer, P.E. 2019. The many secret lives of adipocytes: implications for diabetes. *Diabetologia*. 62:223–232. doi:10.1007/s00125-018-4777-x.

Schopow, N., S. Kallendrusch, S. Gong, F. Rapp, J. Körfer, M. Gericke, N. Spindler, C. Josten, S. Langer, and I. Bechmann. 2020. Examination of ex-vivo viability of human adipose tissue slice culture. *PLoS One*. 15:e0233152-. doi:10.1371/journal.pone.0233152.

Shen, J.X., M. Couchet, J. Dufau, T. de Castro Barbosa, M.H. Ulbrich, M. Helmstädter, A.M. Kemas, R. Zandi Shafagh, M.-A. Marques, J.B. Hansen, N. Mejhert, D. Langin, M. Rydén, and V.M. Lauschke. 2021. 3D Adipose Tissue Culture Links the Organotypic Microenvironment to Improved Adipogenesis. *Advanced Science*. 8:2100106. doi:10.1002/advs.202100106.

Shinde, A.B., A. Song, and Q.A. Wang. 2021. Brown Adipose Tissue Heterogeneity, Energy Metabolism, and Beyond. *Front. Endocrinol. (Lausanne).* Volume 12-2021. doi:10.3389/fendo.2021.651763.

Shinoda, K., I.H.N. Luijten, Y. Hasegawa, H. Hong, S.B. Sonne, M. Kim, R. Xue, M. Chondronikola, A.M. Cypess, Y.-H. Tseng, J. Nedergaard, L.S. Sidossis, and S. Kajimura. 2015. Genetic and functional characterization of clonally derived adult human brown adipocytes. *Nat. Med.* 21:389–394. doi:10.1038/nm.3819.

Silva, G. da N., and A.A. Amato. 2022. Thermogenic adipose tissue aging: Mechanisms and implications. *Front. Cell Dev. Biol.* Volume 10-2022. doi:10.3389/fcell.2022.955612.

Stanford, K.I., R.J.W. Middelbeek, K.L. Townsend, D. An, E.B. Nygaard, K.M. Hitchcox, K.R. Markan, K. Nakano, M.F. Hirshman, Y.-H. Tseng, and L.J. Goodyear. 2012. Brown adipose tissue regulates glucose homeostasis and insulin sensitivity. *J. Clin. Invest.* 123:215–223. doi:10.1172/JCI62308.

Strobel, H.A., T. Gerton, and J.B. Hoying. 2021. Vascularized adipocyte organoid model using isolated human microvessel fragments. *Biofabrication*. 13:35022. doi:10.1088/1758-5090/abe187.

Sun, K., C.M. Kusminski, K. Luby-Phelps, S.B. Spurgin, Y.A. An, Q.A. Wang, W.L. Holland, and P.E. Scherer. 2014. Brown adipose tissue derived VEGF-A modulates cold tolerance and energy expenditure. *Mol. Metab.* 3:474–483. doi:10.1016/j.molmet.2014.03.010.

Virtanen, K.A., M.E. Lidell, J. Orava, M. Heglind, R. Westergren, T. Niemi, M. Taittonen, J. Laine, N.-J. Savisto, S. Enerbäck, and P. Nuutila. 2009. Functional Brown Adipose Tissue in Healthy Adults. *New England Journal of Medicine*. 360:1518–1525. doi:10.1056/NEJMoa0808949.

Wang, O., L. Han, H. Lin, M. Tian, S. Zhang, B. Duan, S. Chung, C. Zhang, X. Lian, Y. Wang, and Y. Lei. 2023. Fabricating 3-dimensional human brown adipose microtissues for transplantation studies. *Bioact. Mater.* 22:518–534. doi:10.1016/j.bioactmat.2022.10.022.

Wolff, A., M. Frank, S. Staehlke, and K. Peters. 2022. A Comparative Study on the Adipogenic Differentiation of Mesenchymal Stem/Stromal Cells in 2D and 3D Culture. *Cells*. 11. doi:10.3390/cells11081313.

Wu, J., P. Cohen, and B.M. Spiegelman. 2013. Adaptive thermogenesis in adipocytes: Is beige the new brown? *Genes Dev.* doi:10.1101/gad.211649.112.

Xue, R., M.D. Lynes, J.M. Dreyfuss, F. Shamsi, T.J. Schulz, H. Zhang, T.L. Huang, K.L. Townsend, Y. Li, H. Takahashi, L.S. Weiner, A.P. White, M.S. Lynes, L.L. Rubin, L.J. Goodyear, A.M. Cypess, and Y.-H. Tseng. 2015. Clonal analyses and gene profiling identify genetic biomarkers of the thermogenic potential of human brown and white preadipocytes. *Nat. Med.* 21:760–768. doi:10.1038/nm.3881.

Yao Xi and Dani, C. 2022. A Simple Method for Generating, Clearing, and Imaging Pre-vascularized 3D Adipospheres Derived from Human iPS Cells. *In* Induced Pluripotent Stem (iPS) Cells: Methods and Protocols . K. Nagy Andras and Turksen, editor. Springer US, New York, NY. 495–507.

Yu, Y., H. Huang, J. Ye, Y. Li, R. Xie, L. Zeng, Y. Huang, T. Zeng, D. Luo, J. Zhong, and W. Peng. 2024. 3D Spheroids Facilitate Differentiation of Human Adipose-Derived Mesenchymal Stem Cells into Hepatocyte-Like Cells via p300-Mediated H3K56 Acetylation. *Stem Cells Transl. Med.* 13:151–165. doi:10.1093/stcltm/szad076.

Zanoni, M., F. Piccinini, C. Arienti, A. Zamagni, S. Santi, R. Polico, A. Bevilacqua, and A. Tesei. 2016. 3D tumor spheroid models for in vitro therapeutic screening: a systematic approach to enhance the biological relevance of data obtained. *Sci. Rep.* 6:19103. doi:10.1038/srep19103.

Zhang, L., J. Avery, A. Yin, A.M. Singh, T.S. Cliff, H. Yin, and S. Dalton. 2020. Generation of Functional Brown Adipocytes from Human Pluripotent Stem Cells via Progression through a Paraxial Mesoderm State. *Cell Stem Cell*. 27:784-797.e11. doi:10.1016/j.stem.2020.07.013.

Appendices

Appendix 1. Reagents, Software and Devices

***Table 3. List of all the reagents, chemicals, software and equipment used in this thesis**.*
Along with their names, the supplier, location and catalog number are also mentioned.

Name	Supplier	Location	Catalog / Identifier
[^{18}F]-Fluorodeoxyglucose	PET Centre	Turku, Finland	—
Acetone	Fisher Chemical	Waltham, Massachusetts, USA	LOT: 254277
Amphotericin B	Gibco, Thermo Fisher Scientific	Massachusetts, USA	#15290018
BioRender	BioRender	Toronto, Ontario, Canada	—
Bovine serum albumin (BSA)	Sigma-Aldrich	Missouri, USA	#A8806
Bovine serum albumin (BSA)	TOCRIS Bioscience	Bristol, United Kingdom	CAS 9048-46-8
cAMP	Sigma-Aldrich	Missouri, USA	#D0267
DAPI	Thermo Fisher Scientific	Massachusetts, USA	#D1306
DMEM/F12	Gibco, Thermo Fisher Scientific	Massachusetts, USA	#11320033
DMSO	Sigma-Aldrich	Missouri, USA	#D8418
D-sorbitol	Sigma-Aldrich	Missouri, USA	CAS 50-70-4
DPBS	Euroclone	Milan, Italy	#ECB4004L
Hoechst 33342	Thermo Fisher Scientific	Massachusetts, USA	#H3570

ImageJ/FIJI	Open source	—	Version 1.54p, Java 1.8.0_322 (64-bit)
Intralipid	Sigma-Aldrich	Missouri, USA	#I141
Insulin, human recombinant	Sigma-Aldrich	Missouri, USA	#I9278
JEM-1400 Plus TEM	JEOL	Akishima, Tokyo, Japan	—
Leica CM3050 S cryostat	Leica Microsystems	Wetzlar, Germany	—
Leica Stellaris 8 Falcon FLIM with FCS and Resonant Scanner	Leica Microsystems	Wetzlar, Germany	—
Methanol	Fisher Chemical	Waltham, Massachusetts, USA	LOT: 2550011
Microsoft Power BI Desktop	Microsoft	Redmond, Washington, USA	Version 2.152.882.0
Olympus Microscope CX21 Binocular Head	Olympus	Hachioji, Tokyo, Japan	—
Penicillin/streptomycin solution (P/S)	Thermo Fisher Scientific	Massachusetts, USA	#15140-122
PFA 4% in PBS	Thermo Scientific	Massachusetts, USA	#J19943.K2
Propidium iodide (PI)	Sigma-Aldrich	Missouri, USA	#P4864
Rosiglitazone	Sigma-Aldrich	Missouri, USA	#R2408
Triton X-100	Sigma-Aldrich	Missouri, USA	CAS 9036-19-5
Trypsin-EDTA (0.5%)	Thermo Fisher Scientific	Massachusetts, USA	#15400054
Tween 20 solution	Bio-Rad Laboratories	Hercules, California, USA	#1610781
VECTASHIELD Vibrance® Antifade Mounting Medium	Vector Laboratories	Newark, California, USA	LOT: WO46163

Vector® TrueVIEW® Autofluorescence Quenching Kit	Vector Laboratories	Newark, California, USA	LOT: WOVUS35070